Project Offshore Deep Slope
Phase II

Progress Report

March 2004

Prepared for:

BP
ChevronTexaco
Encana
ExxonMobil
Minerals Management Service
Murphy
Petro-Canada
Petroleum Research Atlantic Canada

Prepared by:

C-CORE

C-CORE
Morrissey Road
St. John's, NF
Canada A1B 3X5

T: (709) 737-8354
F: (709) 737-4706

Info@ccore.ca
www.c-core.ca

TABLE OF CONTENTS

LIST OF TABLES

LIST OF FIGURES

1.0 INTRODUCTION

Project Offshore Deep Slope (PODS) was initiated to develop a capability to accurately quantify the risks associated with activity on deepwater slope regions. This report presents an update on the activities performed in relation to Phase II of PODS. The report focuses on the 4 centrifuge tests performed and the interpretation of the results. Progress on the development of the risk framework is also reported in detail.

This progress report is intended as a working document and feedback (comments and suggestions) is encouraged from the PODS participants. This would offer the advantage of tapping into the considerable experience and knowledge in the industry and allow priorities and focus areas to be identified to the benefit of the program and its participants.

Four centrifuge tests have been completed and are discussed in detail in this report. Analysis of the tests and further numerical work is ongoing. The development of a risk methodology is proceeding, using data provided by the Geological Survey of Canada for the conditions on the Scotian Slope. A report covering the Scotian Slope geotechnical and geological conditions is included in Appendix B. The work on gas hydrates is primarily a stand-alone task and is being performed in parallel with the other areas of work, to conclude in mid 2004. A University of Calgary progress report covering this task is included in Appendix A. Data gathering for the risk-based tasks are ongoing, with integration of this and other data and methods of analysis to continue to mid-2004. The original date for completion of PODS Phase II was March 31, 2004. However, the later than expected start, and additional funding has resulted in an extension of the workscope, with an anticipated completion date of August 2004.

2.0 CENTRIFUGE TESTS

Physical modeling in the geotechnical centrifuge is used to simulate different potential triggering mechanisms. A number of trigger mechanisms have been selected for centrifuge modeling, based on relevance to offshore conditions and limitations of modeling in the centrifuge.

2.1 General Centrifuge Test Set-up

The PODS centrifuge test models are constructed in a plane strain rectangular strongbox measuring 900mm x 300mm in plan. The box consists of a steel and aluminum frame on three sides supported on a steel base plate. One long side is fitted with a 100mm thick perspex sheet to allow observation of the model during the test using an onboard CCTV.

The strongbox was placed on a plywood wedge inclined at 4^o to the horizontal, maintaining a horizontal surface due to the consistency of the soil slurry, as shown in Figure 1(a). The soil was then consolidated in the centrifuge at 100g acceleration, creating stress conditions consistent with a normally consolidated profile. Progress of consolidation was monitored using a linear voltage displacement transducer (LVDT) on the surface and pore water pressure transducers (PPT) embedded in the soil. On completion of consolidation, the inclined wedge was turned through 180^o below the strongbox. This resulted in the formation of an 8^o soil surface as shown in Figure 1(b). The soil surface maintained the slope due to strength gained during the consolidation initial phase. The model was then replaced into the centrifuge and underwent reconsolidation to reach equilibrium conditions at 100g acceleration.

The package acceleration was increased incrementally to allow excess pore pressures to dissipate at each stage to prevent premature failure of the slope. On reaching 100g, the package is allowed to consolidate fully, again monitored using LVDT and PPT readings. Each consolidation phase took an average of 8 hours.

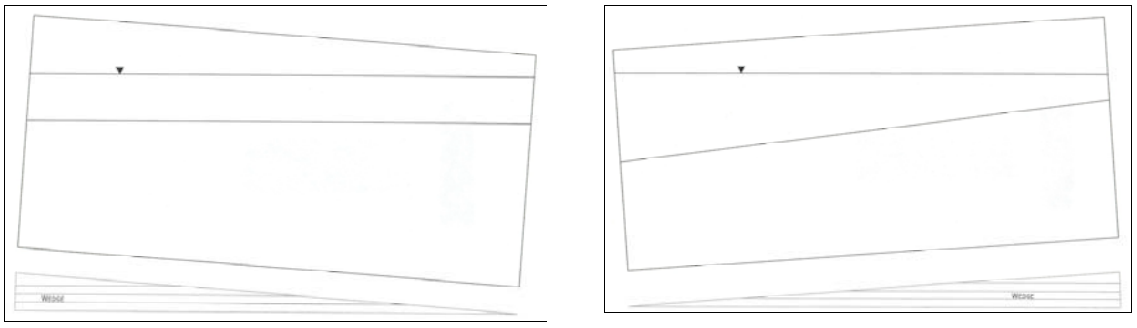

(a) (b)

Figure 1: Method of Test Package Preparation to Form 8^o Slope

This procedure was modified as the testing program proceeded to adapt to the test conditions and reduce centrifuge flight time. Tests 2, 3 and 4 incorporated the presence of a sand layer within the kaolin soil bed and so a three-stage preparation technique was developed. A bottom layer of clay was poured and consolidated in a loading frame at 1g in the laboratory. This provided the soil with enough strength to support the sand layer without excessive mixing or impregnation. The consolidation pressure was selected so that it remained below the final stress conditions in the model at 100g acceleration, to maintain normally consolidated conditions. A 10mm thick sand layer was then added, followed by the top clay layer. The preparation was then continued as described above to achieve the final stress conditions in the centrifuge.

The test package was fitted with headworks bolted to the top of the strongbox. Equipment included cone penetration test (CPT) drive, actuators and motors to drive the various triggering mechanisms to induce slope failure. A system of motor operated valves controlled the water flow to and from the package. The surface water, sand layer (when applicable) and bottom drain were all connected to a standpipe and overflow as water was expelled from the package during consolidation. Water could be added to the surface of the package as required to offset the effects of evaporation. During testing, the valves were closed to prevent water release from the intermediate sand layer during the slope failure trigger event. A typical test package is shown in Figure 2.

Figure 2: Typical PODS Centrifuge Test Package

Instrumentation of the package consisted of LVDTs to measure soil surface movement and PPTs embedded in the soil bed and at critical positions on the equipment. The pore water response during consolidation and loading events were important in determining the response of the slope and resilting mode of failure. The CPT was also instrumented at the tip, sleeve and porous pore pressure element to provide strength data on the soil. A number of spaghetti markers were placed vertically at regular intervals along the length of the package. One row was placed at approximately the centre line of the box, and one row against the plexiglass window. Any soil movement during the test can then observed by considering movement of the softened spaghetti markers, which offer no resistance to soil movement, allowing failure planes to be identified. The row of centerline strands were fitted with solder strips and x-rayed to allow movement to be visualized without disturbing the soil bed. Any difference between the centre and edge markers could then be used to quantify the effects of side wall friction in the test package. The installation of a CCTV system also allowed observation of slope movement through the Perspex window in real time.

All tests were performed at 100g acceleration, with the CPT and trigger mechanism activated on completion of consolidation of the soil. After each test, the profile of the slope was carefully measured and photographed, focusing on any movement of the slope. The soil bed was also tested for shear strength using shear vane equipment and samples taken to construct moisture content profiles.

2.2 Soil Properties

The soil used in the tests was Speswhite kaolin clay. This soil is available in powder form from a highly consistent source, with well-known and controlled properties. Key properties are provided in Table 1, and the grain size distribution is given in Figure 3. The original plan to modify the soil to produce a highly strain softening material was abandoned after initial testing due to the excessive consolidation times associated with the addition of bentonite required to achieve the desired properties. A consolidation time in excess of 48 hours in the centrifuge would have been needed which was considered impractical. The kaolin was mixed under suction at approximately 90% moisture content. This is above the liquid limit and produces a slurry that has the consistency of a thick fluid. The strongbox was prepared with a layer of drainage sand and a thin layer of Vaseline or Teflon spray to minimize the boundary effects of the side walls. The slurry was then poured into the strongbox to create a uniform layer of soil, followed by surface water to prevent drying of the surface.

On completion of consolidation, each model was tested using the CPT, inserted at a rate of 3mm/s. Shear strength was interpreted from the CPT data using standard correlation formulae:

$$q_{kt} = qc + (1\text{-}a)u_b$$

$$c_u = (q_{kt}\text{-}\sigma_v) / N_{kt}$$

Where: qc is the measured cone tip resistance
A is the cone net area ratio (0.52 in this case)
u_b is the pore pressure acting on the cone tip
σ_v is the total vertical stress acting on the cone tip
N_{kt} is the cone factor for shear strength interpretation

Table 1: Physical properties of Speswhite Kaolin (from Lin 1995)

Property	Units	Value
Clay Content (<2μm)	(%)	75
Mean Grain Size, D_{50}	mm	0.0005
Plastic Limit	(%)	35
Liquid Limit	(%)	65
Plasticity Index	(%)	30
Specific Gravity	(-)	2.62
Permeability	(m/s)	0.5 to 2.0 x 10^{-9}
Coefficient of Consolidation	(mm^2/s)	0.1 to 0.5

An N_{kt} value of 10.66 was applied to obtain the shear strength profile, based on experience of testing normally consolidated kaolin test beds at C-CORE. Values quoted by other researchers range from 5 to 12, depending on test conditions, cone type and calibration against other testing methods. Vane test results were also performed and compared to the CPT results, and generally show a lower shear strength. This is normal, since the tests are carried out after the test under 1g, after the soil has undergone some swelling and softening as overburden pressure is removed.

Figure 4 shows a composite plot of the CPT results for each of the 4 test packages. Test 1 was prepared using a slurry at 65% moisture content compared to 90% in tests 2 to 4. This low moisture content was initially used to provide sufficient strength to allow LVDTs to measure surface settlement without embedding themselves into the slurry. The resulting shear strength was, however, greater than targeted, suggesting n effectively over-consolidated profile near the surface. Subsequent tests were therefore mixed at 90% to ensure a normally consolidated profile. The effect of the sand layer in Tests 2 to 4 is evident, with sharp increases in cone resistance at the level of the sand layer.

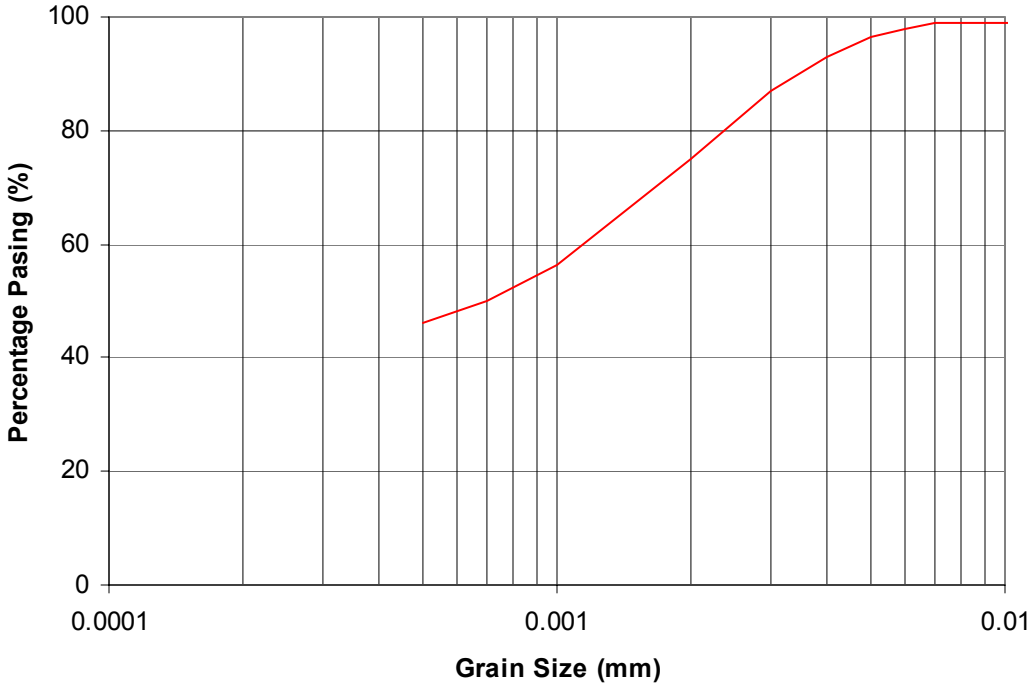

Figure 3: Grain Size Distribution for Speswhite Kaolin

Figure 5 shows the interpreted shear strength profile from CPT data and vane test results for each test. Interpretation of shear strength can be unreliable at shallow depths of less than about 4 cone diameters due to differences in penetration mechanism, and so the data provided serves primarily to illustrate consistency in soil strength between tests. A reference line is also included in Figure 6, giving a ratio of 0.2 between shear strength and overburden pressure. The value of 0.2 is commonly referenced for normally consolidated clay, although a range of values is often quoted. Almeida, M.S. and Parry, R.H. (1985), for example quote 0.226 for normally consolidated kaolin clay.

The moisture content profile of each testbed was also used to provide interpretation of the soil conditions. Figure 6 is a composite plot relating moisture content to shear strength interpreted from CPTs and vane tests. An overall relationship was developed to provide a consistent approach to interpretation.

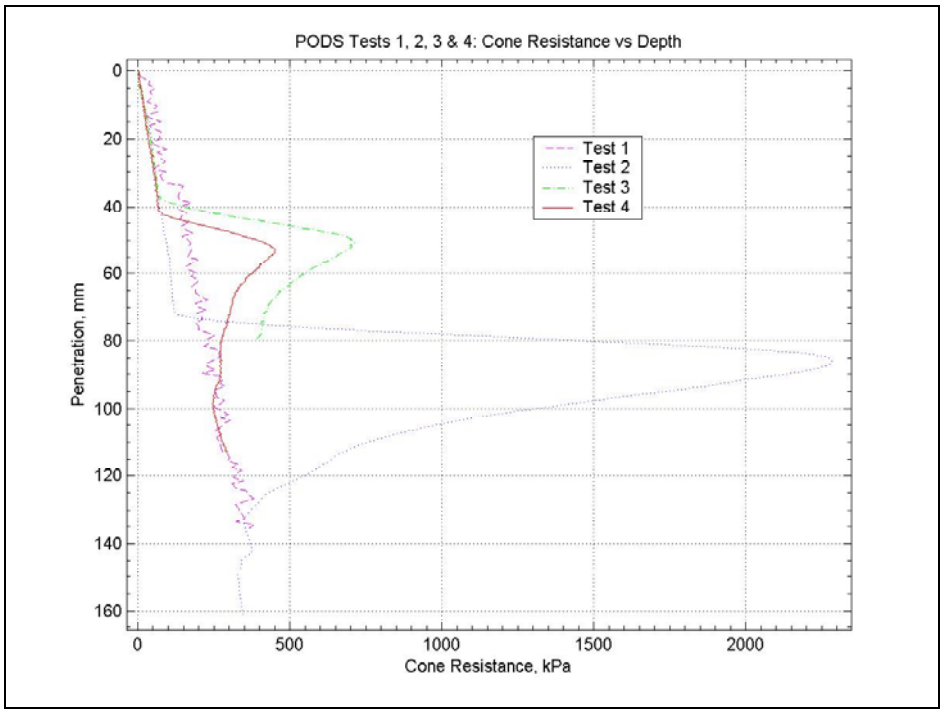

Figure 4: Composite Plot of CPT Cone Resistance

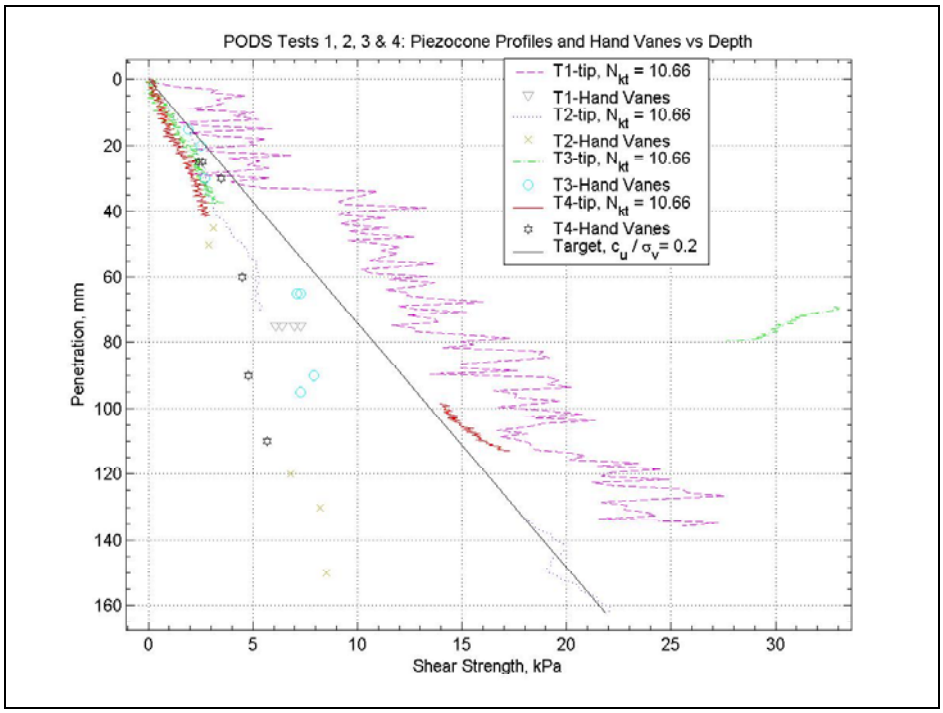

Figure 5: Composite Plot of Interpretted Shear Strength from CPT and Vane Data

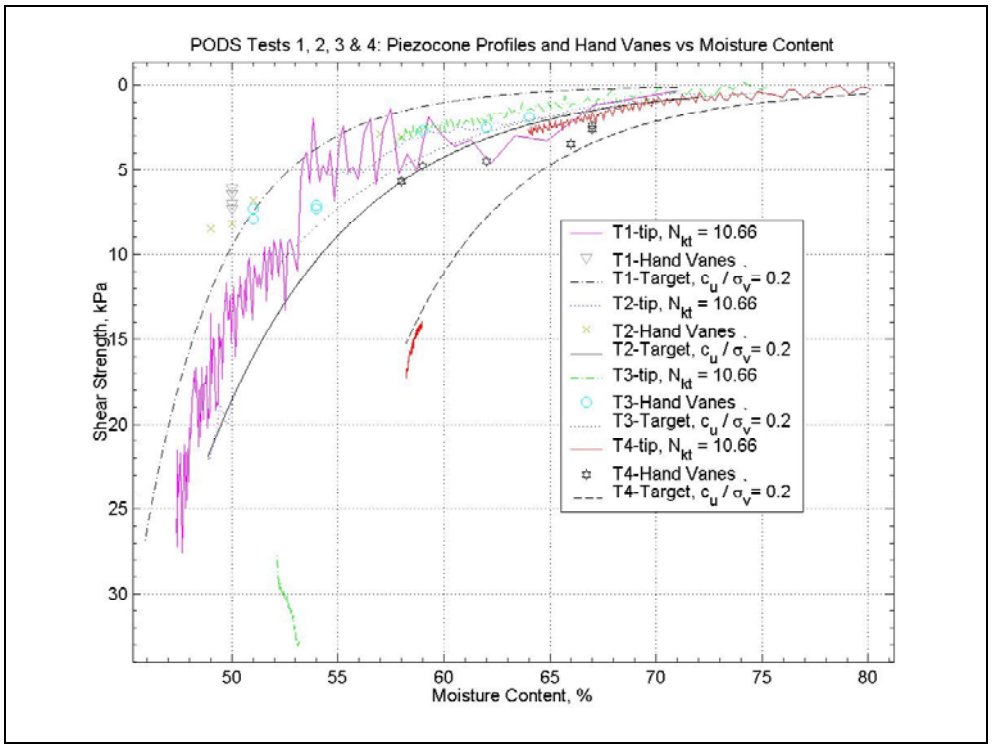

Figure 6: Plot of Shear Strength vs. Moisture Content

2.3 Test 1 Discussion

Test 1 was aimed at investigating the effect of erosion at the toe of the slope, and also the effect of a adding a surcharge at the crest. Large erosion features have been observed in a number of regions where on-bottom currents are present and so there is a real possibility of over-steepening and initiation of slope instability. Loading of the crest of a slope may be a result of high rates of sedimentation, whereby increased pore water pressure exceeds the rate of dissipation.

The initial configuration of the centrifuge model during the first stage of consolidation is illustrated in Figure 7, showing the position of the LVDT, toe injector, and PPTs, but excluding headworks such as vertical actuators and the piezocone.

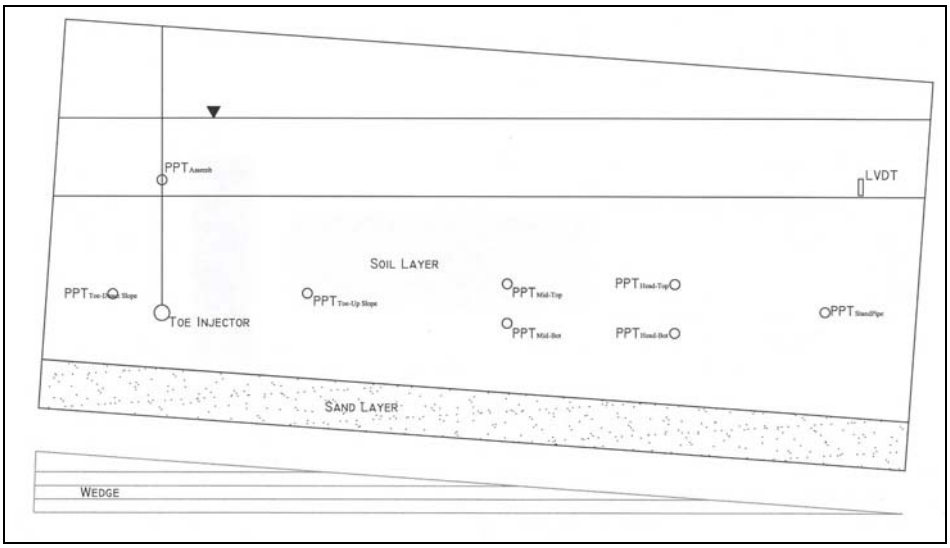

Figure 7: Test 1 Profile View of Phase 1 Consolidation Configuration.

On completion of the first phase consolidation, the head of the slope was cut back to provide a horizontal surface for the LVDT and the bearing plate. The package was turned on the wedge to create the 8^{o} slope as shown in Figure 8.

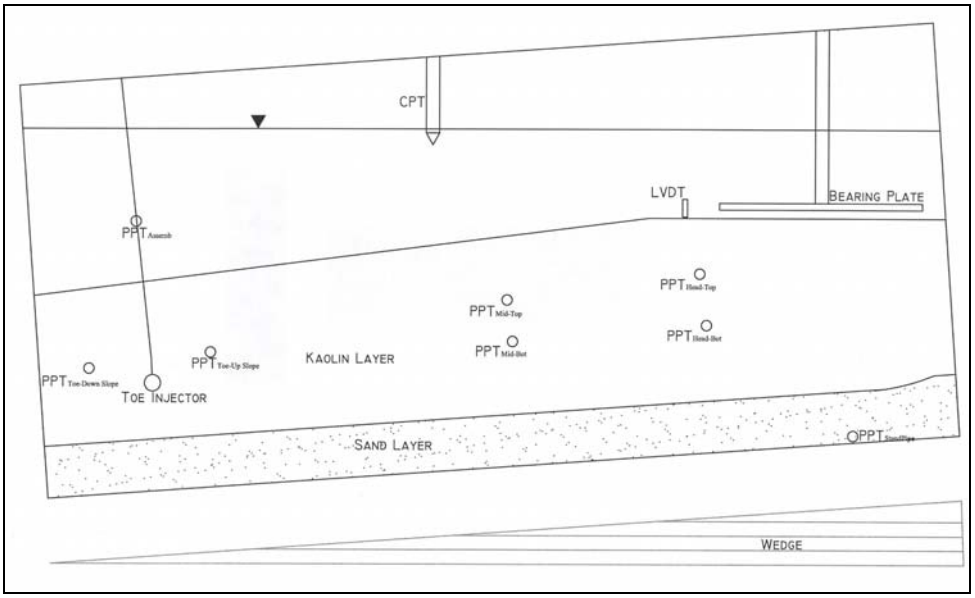

Figure 8: Test 1 profile view of phase 2 configuration.

The toe erosion mechanism was used as a primary trigger and was a development of the toe injection system used in the PODS Phase 1 demonstration tests. It consisted of a 12.7mm diameter buried pipe connected to a high-pressure water supply and lifting mechanism. Water injection through a number of 0.8mm diameter holes was intended to liquefy the clay above the buried pipe, effectively producing a near vertical face at the toe of the slope. Simultaneously raising the pipe was intended to create a trenched erosion feature that would remove support of the toe of the slope and lead to failure.

Once the water pressure was applied, it was found that the injected water created short-circuiting paths to the soil surface, rather than causing general fluidising of the clay in the vicinity. Figure 9 presents the pore pressure measurements during this phase of the test, with each PPT labeled according to its position in given in Figure 8. The linear increase of PPT_{Assemb} in Figure 9 indicates the addition of surface water due to water short-circuiting from the pipe. In Figure 10 which shows excess pore water above hydrostatic conditions for each PPT, the initial increase of excess pore pressures in $PPT_{Toe\text{-}Downslope}$ and $PPT_{Toe\text{-}Upslope}$ at position A demonstrates the injection of water. The time scale in Figures 9 and 10 is based on the complete centrifuge test, including the two phases of consolidation, the CPT, and slope failure testing.

With the injection water remaining on, the toe injector was pulled vertically approximately 30mm at a rate of 1mm/s, which did not cause slope failure. It is considered likely that the gap behind the pipe was quickly filled with slurry as it flowed around the pipe as it was pulled upward. Movement of the toe injector is represented by the decrease in pore pressure of PPT_{Assemb} between positions B and C in Figures 9 and 10. The toe injector was stopped and the water turned off at position C.

Although there was no slope failure due to the movement of the toe injector, there were significant excess pore pressure responses at $PPT_{Toe\text{-}Downslope}$ and $PPT_{Toe\text{-}Upslope}$ at position C in Figure 9, indicating some response within the slpe, although insufficient to cause failure.

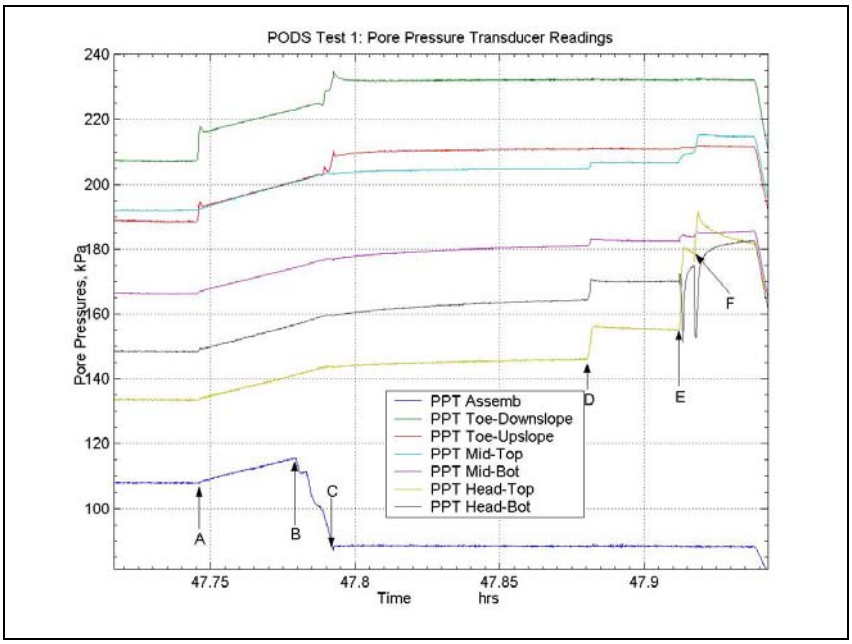

Figure 9: Pore pressure transducer readings of test 1.

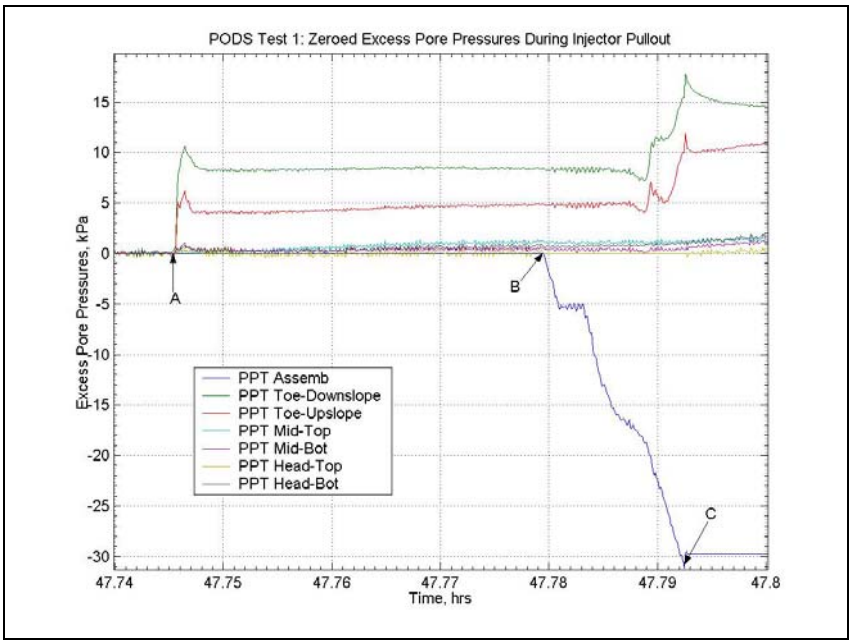

Figure 10: Zeroed excess pore pressures of test 1 during toe injector pullout.

The PODS Phase 1 demonstration tests used a sand dumping technique to load the crest of the slope, whereby a tray of sand was tipped at the required position at the top of the slope. Control and measurement of the applied load was difficult however, and the dynamic effects of the sand impacting the soft clay surface made interpretation difficult. In order to overcome these difficulties, a loading plate was designed, that could be lowered at a constant rate, with applied load measured using a load cell.

Loading of the crest of the slope using the bearing plate was used as a back-up to the toe erosion process. The bearing plate is an aluminium plate 198 mm x 284 mm in plan with a thickness of 5 mm. Rib strengthening was incorporated to prevent flexure during loading. A 10kN load cell was connected above the plate to record the applied load. The soil surface was loaded in three increments, shown labeled as A, B, and C of Figure 11. The total loading displacement into the soil was approximately 15 mm. The pore pressures response due to the plate loading increments can also be seen at positions A, B, and C of Figure 12.

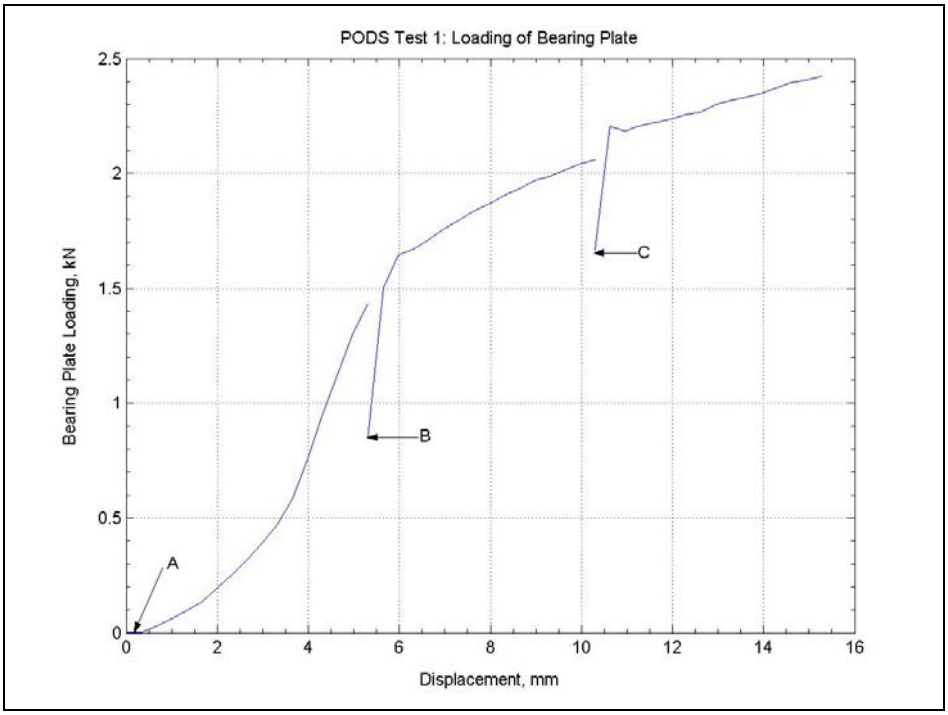

Figure 11: Loading of bearing plate on head of the slope.

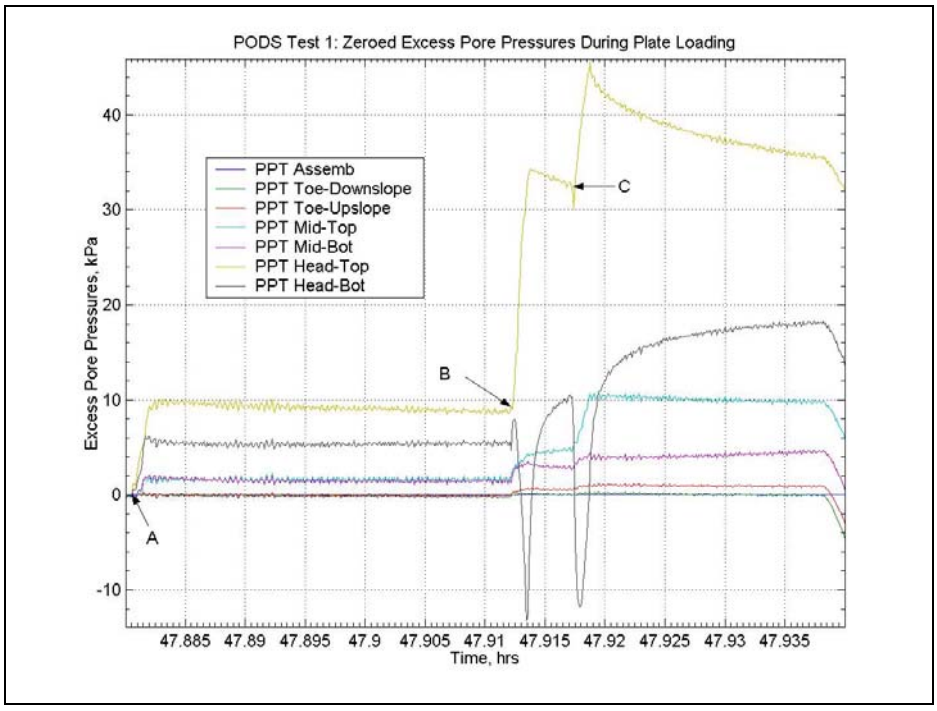

Figure 12: Zeroed excess pore pressures of test 1 during bearing plate loading.

The data in Figures 11 and 12 suggests that the soil beneath the plate failed during loading events B and C. The resistance load continued to increase as the test progressed suggesting that the slope instability did not occur. Shearing did take place, however, as shown by the pore pressure response in the two head PPTs directly below the plate. Figure 13 shows the response of the LVDT placed just in front of the plate, between it and the crest of the slope. The upward movement is consistent with a bearing capacity mechanism rather than a slope failure. Observation of spaghetti movement was inconclusive and no obvious shear plane was identified, as shown in Figure 14.

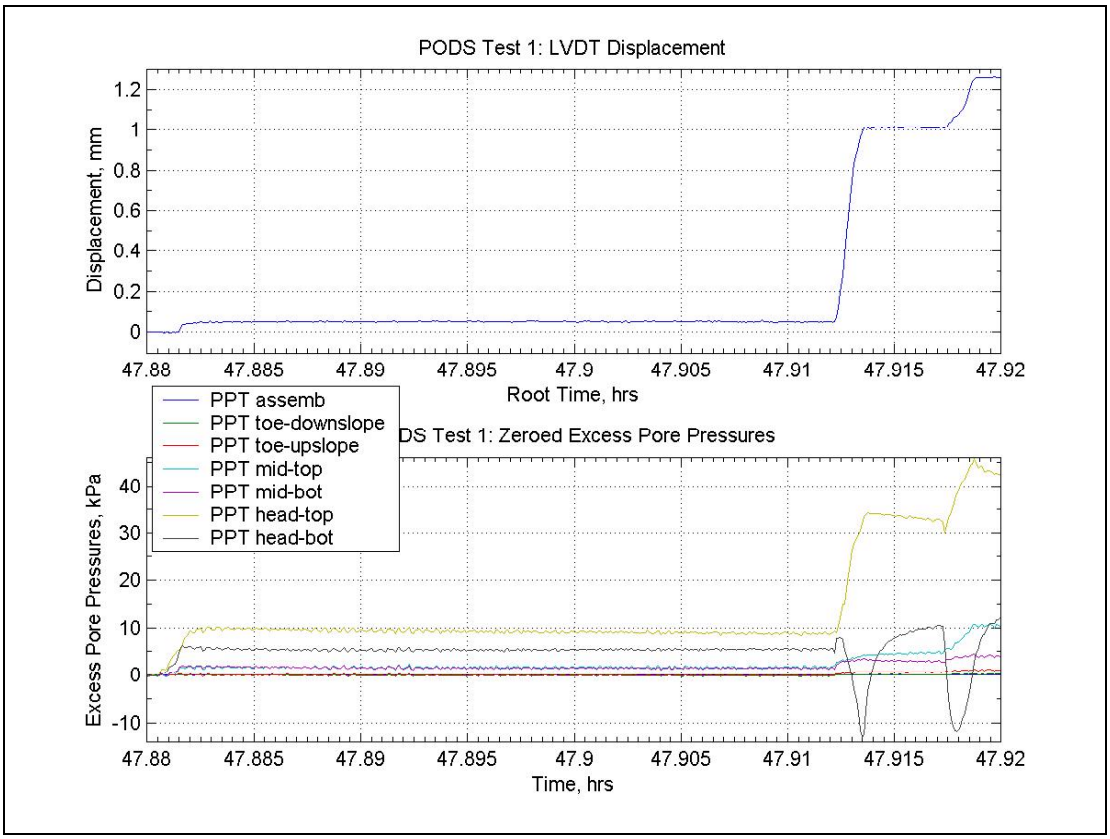

Figure 13: LVDT Readings during Plate Load Application

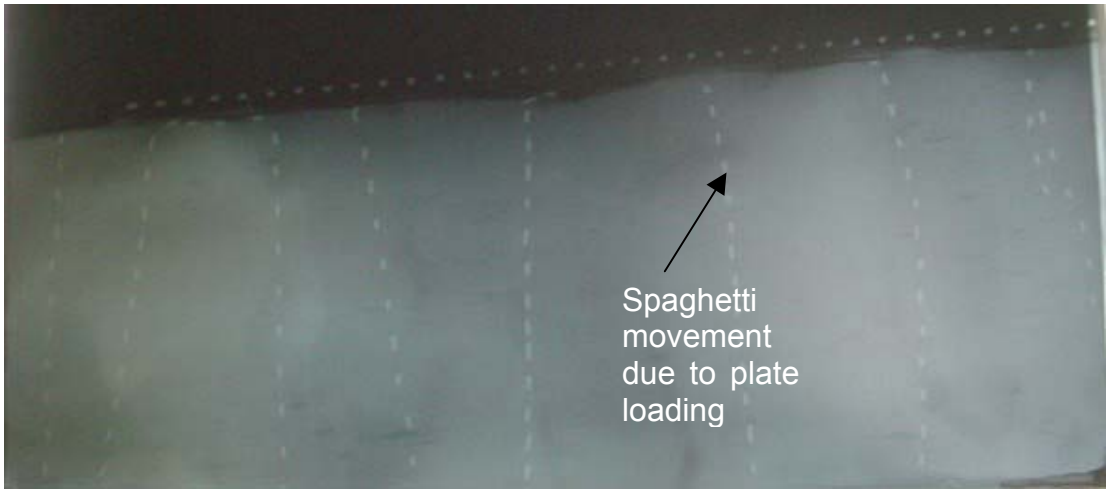

Figure 14: X-ray image of middle of slope.

Bearing capacity calculations for the plate suggest that this may have been the preferred mode of failure in these conditions. Using the Prandtl solution for undrained bearing capacity calculation, modified to account for the increasing shear strength with depth, a capacity of 2.4kN is obtained using:

$$Q_f = R[5.14 + mB/4s_o]s_oA$$

Where: Q_f is the bearing capacity of the plate
R is an empirical factor to account for increasing shear strength with depth (from David & Booker 1973)
m is the rate of increase of shear strength with depth
B is the width of the plate
s_o is the shear strength at the soil surface
A is the plate area

The value of R depends on the ratio of mB/s_o. For conditions in this centrifuge test, a value of R = 1.6 is reasonable, although it should be noted that the large increase of shear strength in relation to the initial value at the soil surface and size of plate footing may lead to some inaccuracy in determining the value R. Nontheless, this suggests that the maximum measured comparable with load is the calculated bearing capacity.

Meyerhof (1957) investigated the relationship between bearing capacity and slope failure as a function of foundation size, slope height, soil shear strength and placement of foundation in relation to the crest of the slope. Theoretical analyses suggest that the capacity of a foundation placed at the crest of an 8^o slope reduces by less than 10% for a uniform soil. For footings set back at distances greater than half of the footing width, the footing capacity can be considered to be a horizontal surface for a 10^o slope. A correlation was also made relating the height of the slope to the soil unit weight and shear strength. This can have large implications on the stability of high, steep slopes, but in the case of relatively shallow cohesive slopes, it is considered that these effects are not significant. Figure15 presents data from Meyerhof (1957).

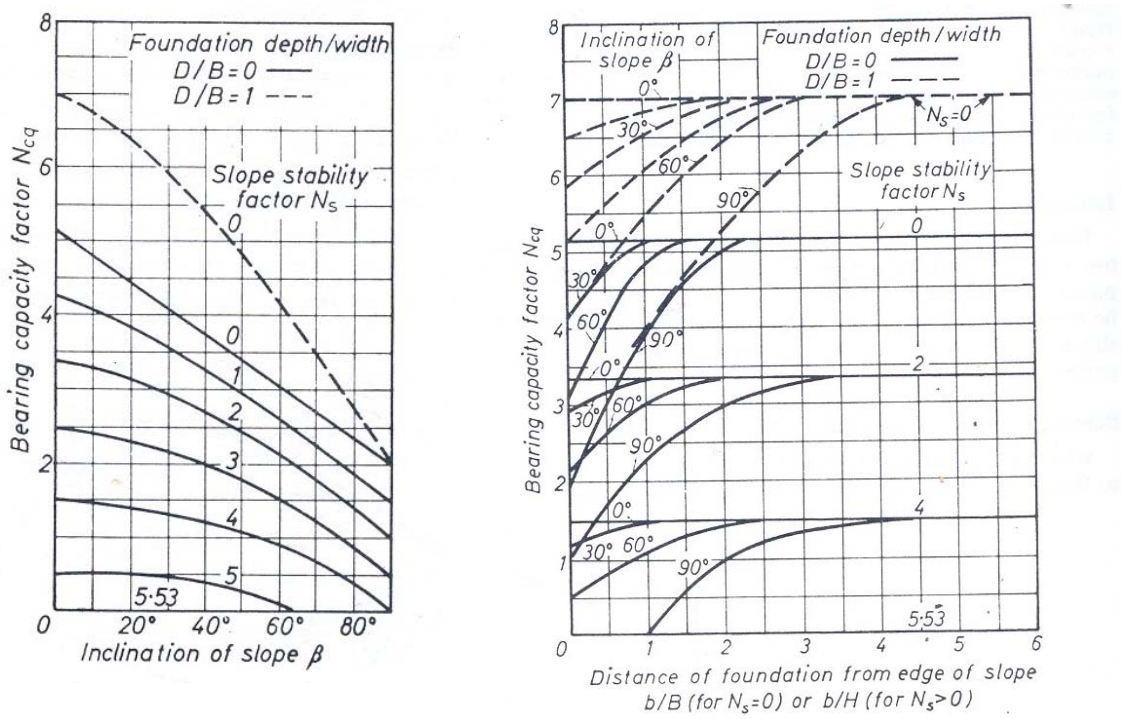

Figure 15: Plots of Relationship between Bearing Capacity Factor, Slope Angle and Distance from Crest of Slope

A limit equilibrium analysis of the slope stability was also performed using undrained strength parameters. The commercially available software, Geoslope SLOPE/W Version 5 was used to predict the response of the slope considering the surface load from the bearing plate. The maximum load from the bearing plate, 2.4 kN, results in a vertical pressure of 42.7 kPa. This pressure is applied using the 'pressure lines' option in SLOPE/W. A soil strength is considered to be increased with depth as $c_u / \sigma'_v = 0.2$.

As shown in Figure 16(a) the minimum factor of safety for the configuration and load applied to the slope in the centrifuge test is 1.17, indicating that failure of the slope is not initiated with this surface pressure. The bearing plate was not placed directly at the crest of the slope in order to allow room for placement of the LVDT to measure settlement during consolidation and response during plate loading. In order to examine the effects of bearing plate location on the stability of the slope, a further analysis was performed for the case of the bearing plate just at the crest of the slope. Other conditions are same as the previous analysis. As shown in Figure 16(b) the factor of safety in this case is 0.98, suggesting that the slope would just fail. It should be noted here that $c_u / \sigma'_v = 0.2$ has been used in this analysis, while the CPT tests in Figure 5 shows potentially higher strength, which would increase the factor of safety above the calculated values.

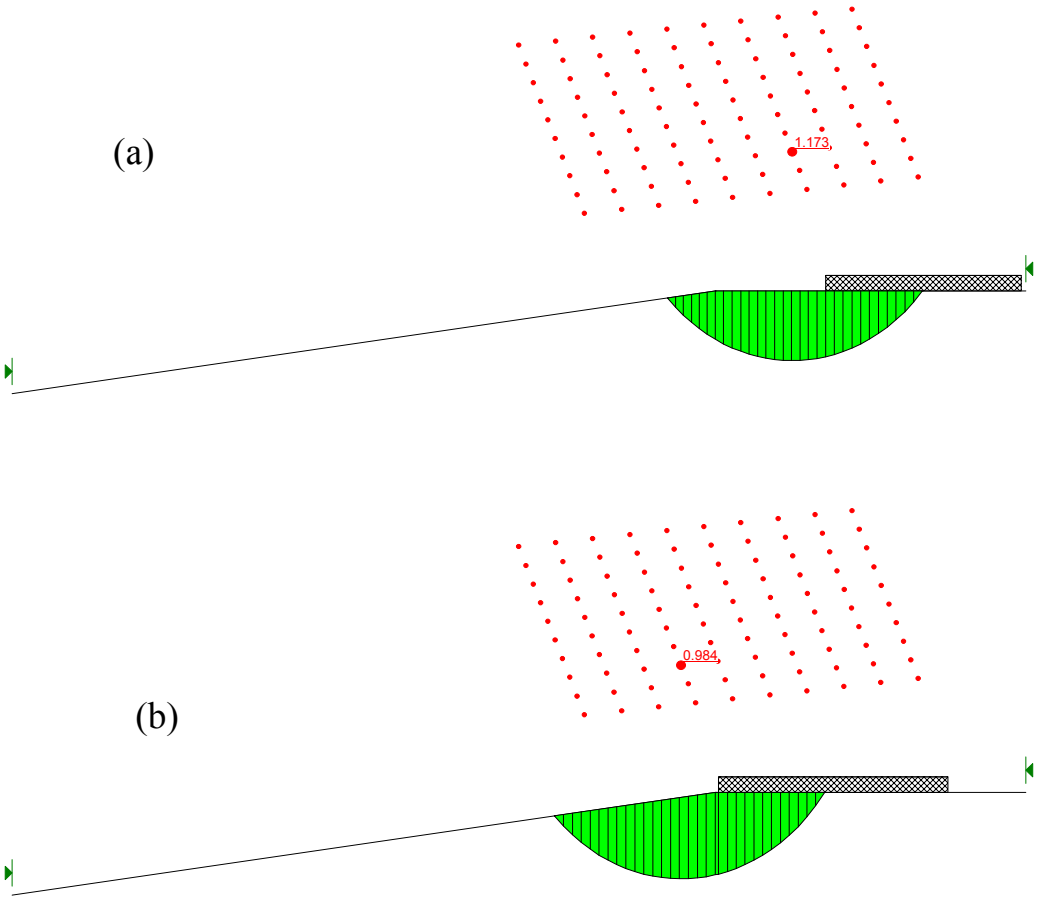

Figure 16: Numerical Analysis using SLOPE/W - Test 1

The test data therefore suggests that the soil filed in bearing capacity rather than by initiation of a slope failure, and that surface loading foundations in soft cohesive soil at the crest of relatively shallow slopes may not be critical to slope stability.

Areas of high sedimentation rates, where large areas are covered by fine-grained deposits, would be unlikely to undergo bearing capacity failure in the way of a foundation of limited plan area. If the sedimentation and existing seabed soil both exhibit low coefficients of consolidation, it is possible that a sufficient stress increment could destabilize the slope quicker than pore pressure dissipation and strength gain. However, such high build-up rates are likely to be confined to very limited locations.

2.3 Test 2 Discussion

The aim of test 2 was to repeat the simulation of toe erosion of the slope. The technique was modified to ensure that support was completely eliminated from the base of the slope and that a near vertical face was formed. An aluminium wedge was fabricated and embedded in the toe of the slope to replace the toe injector mechanism. The wedge geometry was such that it moved away from the upslope side as it was lifted, exposing an unsupported face. A sand layer was also incorporated into the model to trial the procedure proposed for tests 3 and 4. A 3-stage consolidation procedure was therefore followed that allowed the lower clay layer to be pre-consolidated.

The initial configuration of the centrifuge model is illustrated in Figure 17. Figure 17 also shows the soil cross-section and the positions of the LVDT, aluminium wedge, and PPTs, but excludes the headworks such as the vertical actuator and piezocone. Figures 18 and 19 show the configuration of the test package after addition of the sand layer and top layer of slurry, and after rotation of the base wedge to create the 8^{o} slope.

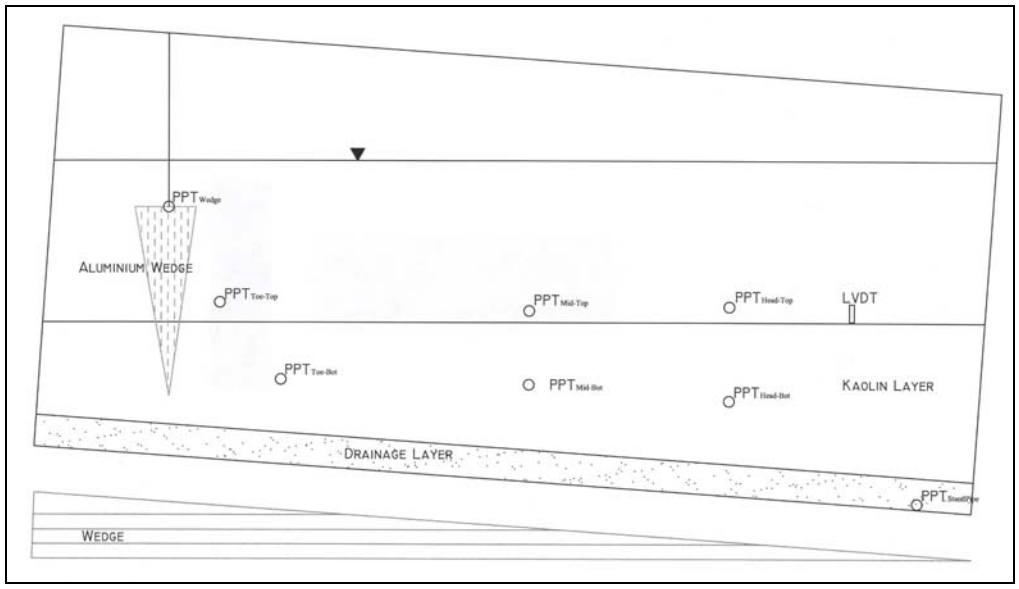

Figure 17: Test 2 profile view of phase 1 configuration.

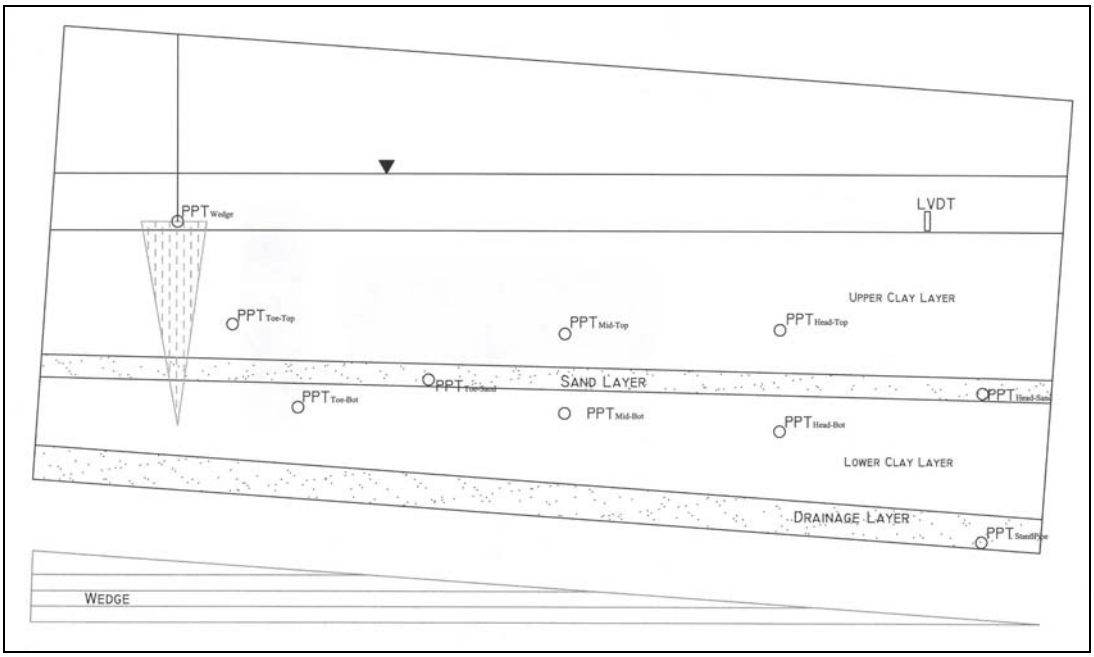

Figure 18: Test 2 profile view of phase 2 configuration.

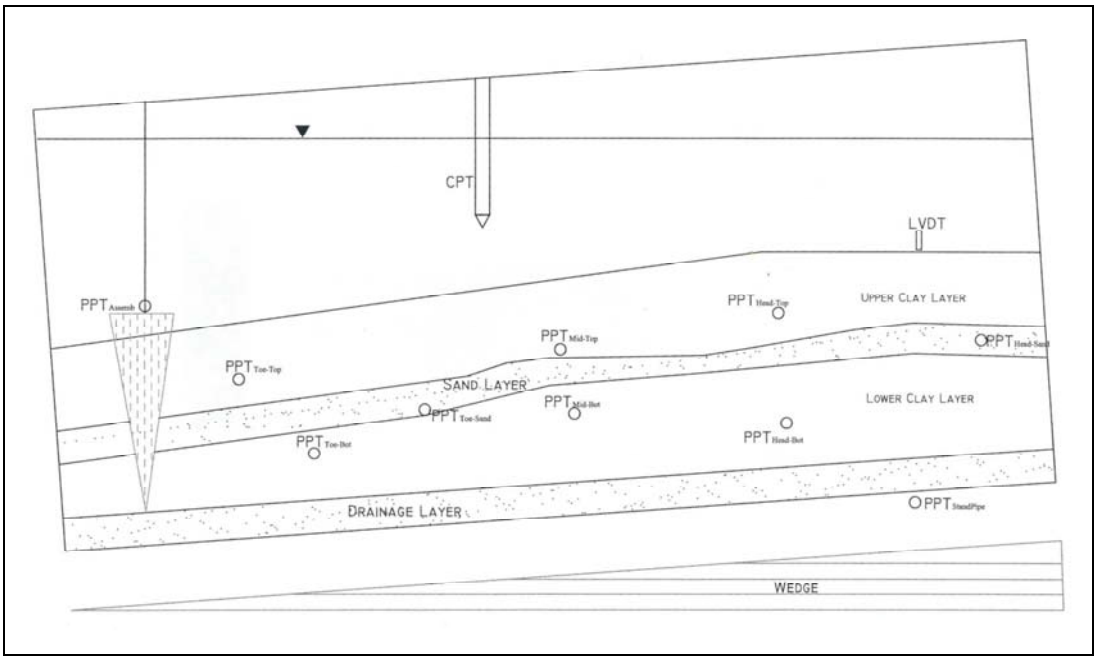

Figure 19: Test 2 Profile View of Phase 3 Configuration

The aluminium wedge was constructed to create a hollow structure filled with sand to ensure its density was greater than the soil. The cross-section dimensions were 180 mm x 180 mm x 63 mm, with a depth (normal to the viewing window) of 295 mm. It was coated with a 2mm layer of Vaseline to reduce side friction and suction forces, and was embedded into the toe of the slope. The wedge was lifted using the same servo-motor system that was used for the toe injector in test 1.

On completion of the consolidation phases, slope failure was initiated by extraction of the aluminium wedge at a constant rate of 2.5mm/s. Figure 20 shows the PPT response as the wedge is extracted. Vertical movement of the aluminium wedge can be seen at position A as the pressure measured by PPT_{Wedge} decreases as it rises through the water column. $PPT_{Toe\text{-}Top}$ and $PPT_{Toe\text{-}Bot}$, nearest to the wedge show significant pore pressure response as the wedge is removed. At point B the wedge was completely extracted from the soil and the servo-motor was turned off.

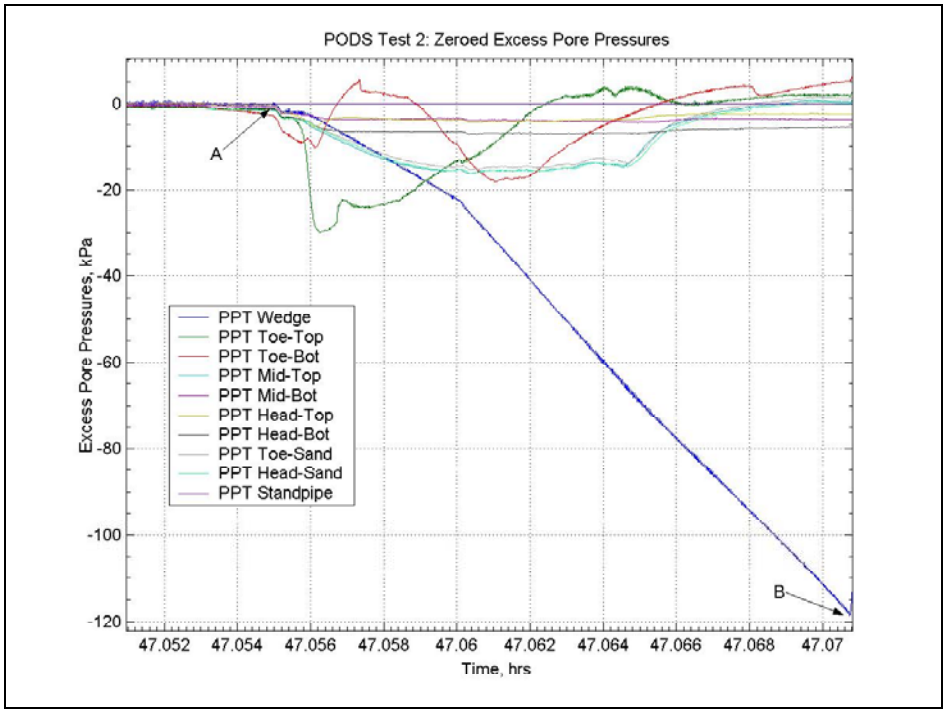

Figure 20: Zeroed excess pore pressures during aluminium wedge pullout of test 2.

Figure 21 shows the final surface expression as the result of soil movement during the test, with surface disturbance clearly visible in the lower part of the slope. A quantity of remoulded clay was also observed to have accumulated at the base of the slope.

Soil movement was inferred from distortion of the spaghetti markers along the Perspex wall of the strongbox, as well as by x-raying the central line of markers. This is shown in

Figures 22 and 23 respectively. Lines were drawn on the Perspex window before the test to indicate the initial position of the markers, with the final position highlighted. The final position of the markers suggests a flow type movement rather than rigid block rotation along a failure plane, although a distinct depth limit can be established near the top of the sand layer. The top of the zone of soil movement corresponds approximately with the position of the CPT, and a slight curvature can be seen at that position. It is therefore considered possible that disturbance associated with this cone penetration may have been enough to create a weakness in the soil structure and define the extent of the mass soil movement.

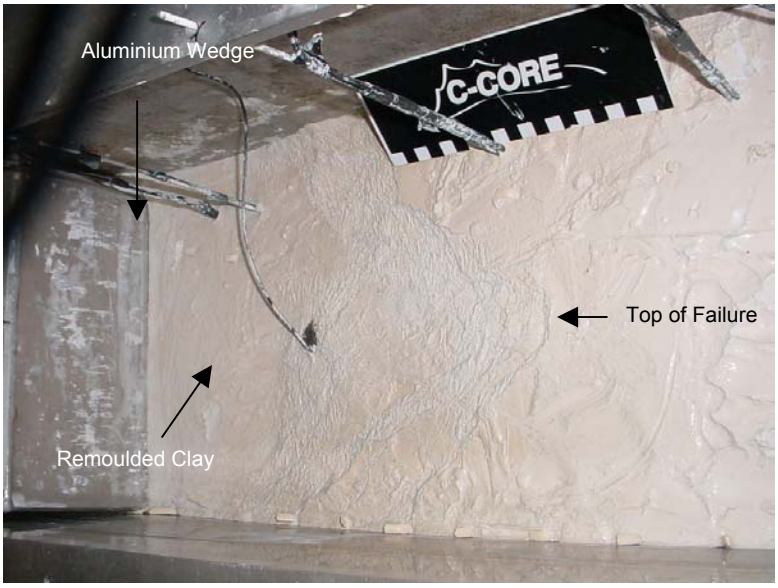

Figure 21: Photo of soil surface after slope failure in Test 2.

Figure 22: Photo of toe of slope after slope failure in test 2.

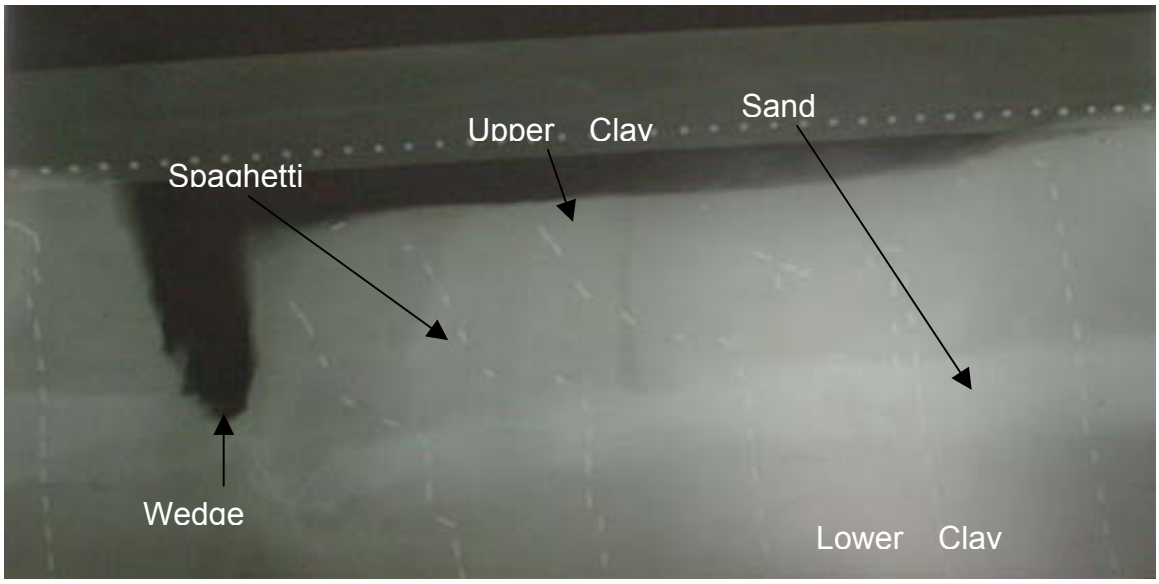

Figure 23: X-ray image of toe of slope in Test 2.

The original position of the wedge is also visible in the x-ray, although soil had moved to close the gap made as it was lifted out. This suggests that remoulded soil can be identified using x-ray techniques, although this is not as clear in other parts of the soil model. A potiluted shear plane, indicative of the base of the mass-movement is shown in Figure 24. The shape of the surface was constructed from spaghetti marker positions in the viewing window and central x-rayed section. The markers suggest that there was some movement within the sand layer, which would be due to loss of support as the wedge was withdrawn.

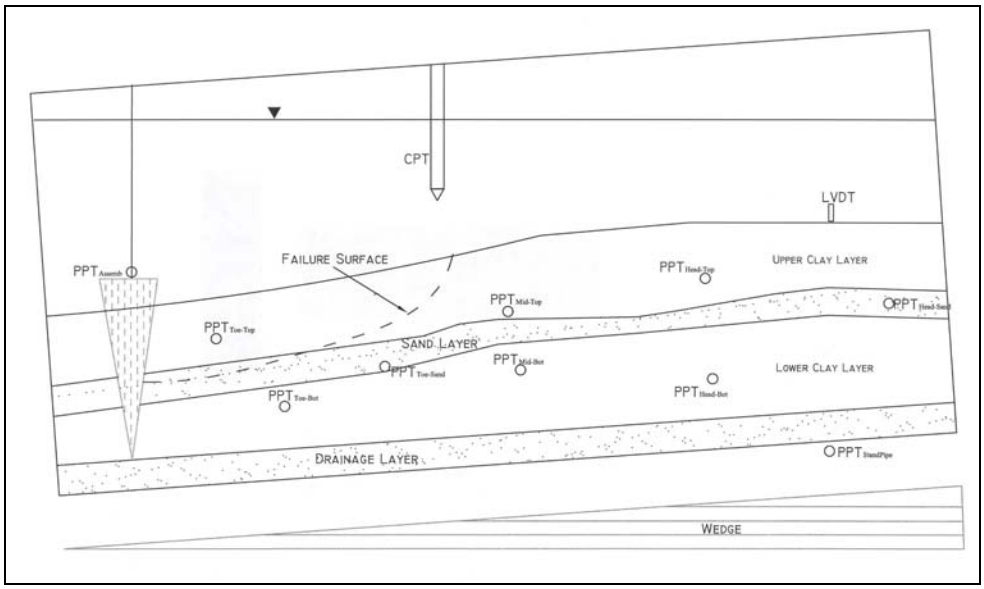

Figure 24: Test 2 profile view of Phase 3 after slope failure.

The test configuration was analysed using limit equilibrium methods in Geoslope's SLOPE/W software. The initial geometry was considered, and a number of failure planes generated corresponding to a range of calculated factors of safety. The generation of slip planes was limited in depth to the top of the sand layer. Figure 25 shows the resulting slip circle generation with associated factors of safety. It is expected that the sudden loss of support at the face would cause a retrogressive type failure, in which an almost vertical slip surface develops and fails into the trench left by the wedge. The resulting profile is still unstable and so further failures are generated until the resulting geometry is stable. This is represented by the surface having a factor of safety of one in Figure 25. The mechanism and exact sequence is unclear, but the above description appears to be consistent with the observed final marker positions.

The analysis was performed using a shear strength profile of $c_u/\sigma_v' = 0.2$. The sensitivity of the shear strength profile used in the analysis was investigated by applying a range of strengths to ascertain the final geometry. A shear strength ratio of $c_u/\sigma_v' = 0.23$ compares well with the observed centrifuge test behaviour, indicating that this analysis provides a reasonable interpretation of the observed mechanism.

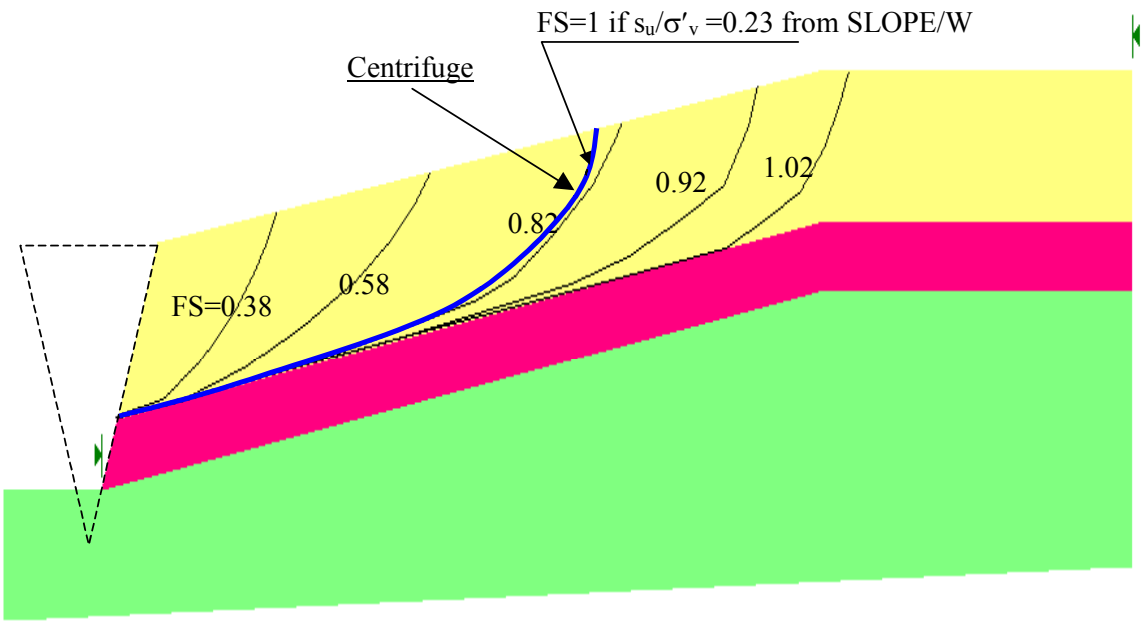

Figure 25: Numerical Analysis using SLOPE/W - Test 2

2.4 Test 3 Discussion

Tests 3 and 4 were performed specifically to investigate the influence of a sand layer within the clay matrix. There is evidence that such layering systems exist in many deepwater offshore locations, and in certain circumstances they may be considered a weak point in the soil profile at which slope instability could be initiated. In particular, the effect of increased pore water pressure within distinct sand layers could lead to loss of effective strength. The cause of increased pore pressure may be earthquakes, release of shallow gas or dissociation of gas hydrates.

The model was constructed with the presence of a 10mm thick sand layer within the silty clay matrix. The initial configuration of the centrifuge model is illustrated in Figure 26, which also displays the soil cross-section and the positions of the LVDT and PPTs.

The lower clay layer was consolidated in the laboratory using a consolidation frame to reduce the flight time in the centrifuge. The sand layer and upper clay layer was then placed and the soilbed consolidated in the centrifuge to reach equilibrium conditions. Figure 21 shows the final condition of the model prior to testing. The top and bottom of the slope was leveled to provide a distinct crest and toe, which would aid interpretation of the test results.

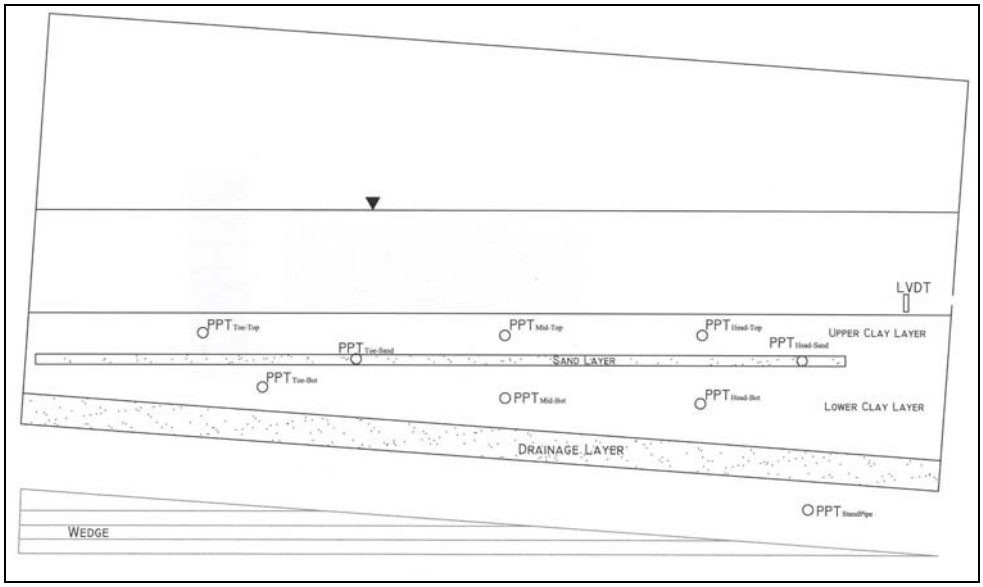

Figure 26: Test 3 profile view of phase 2 configuration.

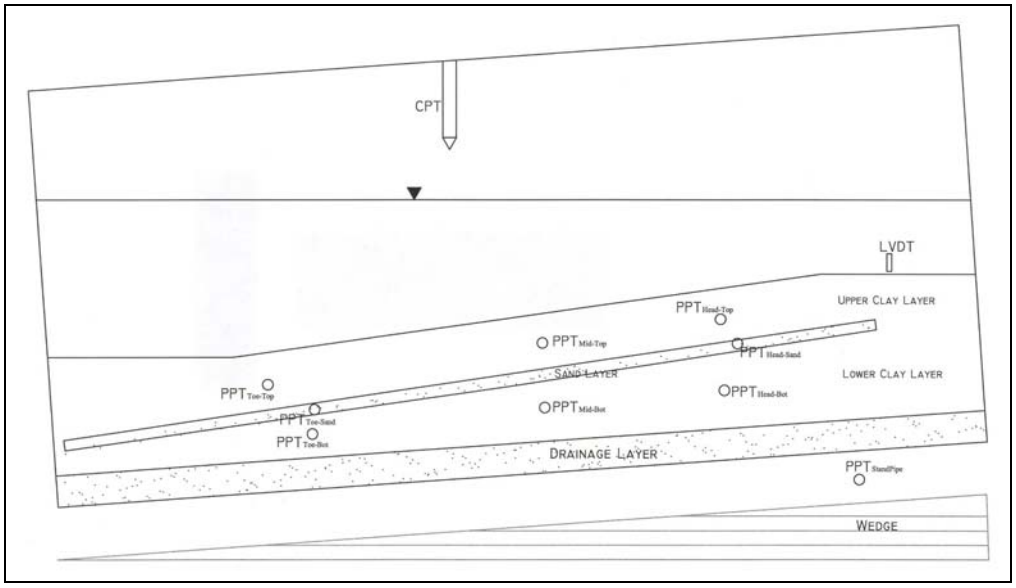

Figure 27: Test 3 profile view of phase 3 configuration.

The sand layer was connected to a water source through a 3-way valve which isolated it from the surface and drain, and connected to the separate water source. A small-diameter perforated flexible hose was embedded in the sand and passed through the strongbox wall at a standard port opening. A head-leveling device located outside the strongbox controlled the pressure applied to the sand layer by raising or lowering using a winch assembly. The position of the head-leveller at any stage suring the testwas obtained by a string potentiometer located at the winch. At the start of the test, the head-leveller was at the approximate level of the water in the strongbox, providing equal pressure inside and out. A valve was opened to connect the sand layer to the head leveler to conduct the test.

The valve was opened at position A in figure 28. As the applied water pressure was increased, pressure in the sand layer underwent a corresponding increase, which continued to point B. Smaller increases in pore pressure in the clay layers were also recorded. The pressurization of the sand layer can easy be seen by the large pore pressure responses of $PPT_{Toe\text{-}Sand}$ and $PPT_{Head\text{-}Sand}$. The subsequent decrease in pore pressures of $PPT_{Mid\text{-}Bot}$ can be attributed to possible soil shearing. At position C another failure event occurred, which can be confirmed by corresponding LVDT displacements as seen in Figure 29 in which settlement of the soil surface at the top of the slope was measured. Compared to the first failure event at position B, larger strains were observed for the second failure event. Also at position C, the short-circuiting of pressurized water from the sand layer to the surface water occurred, evidenced by the sudden observation of a sediment cloud in the surface water. This limited the pressures of the injected water in the sand layer, causing it to drop off at position D.

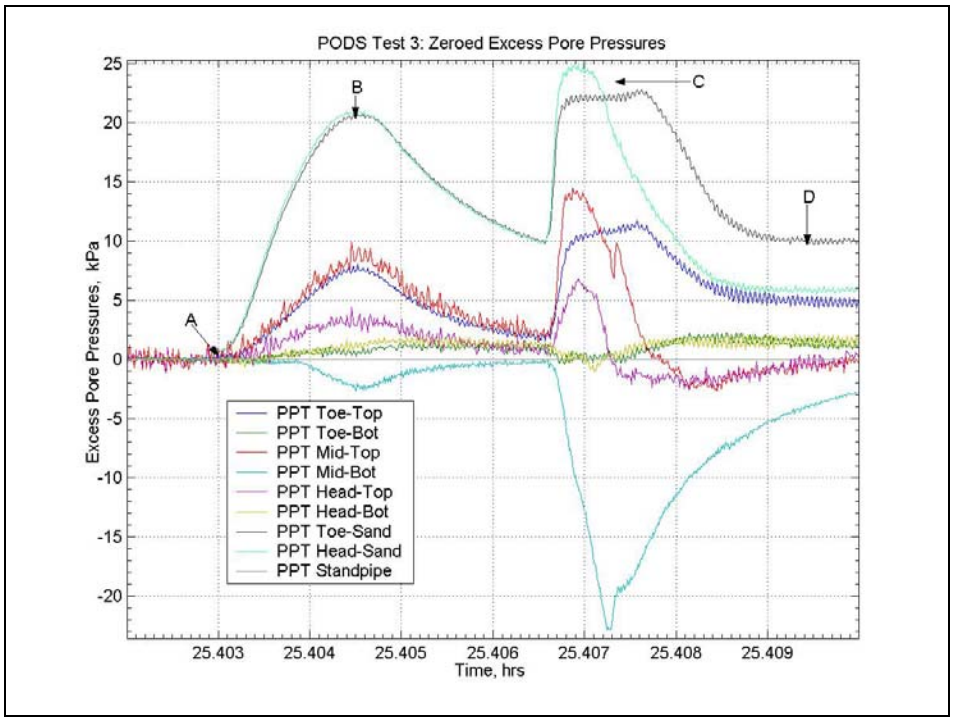

Figure 28: Zeroed excess pore pressures during test 3.

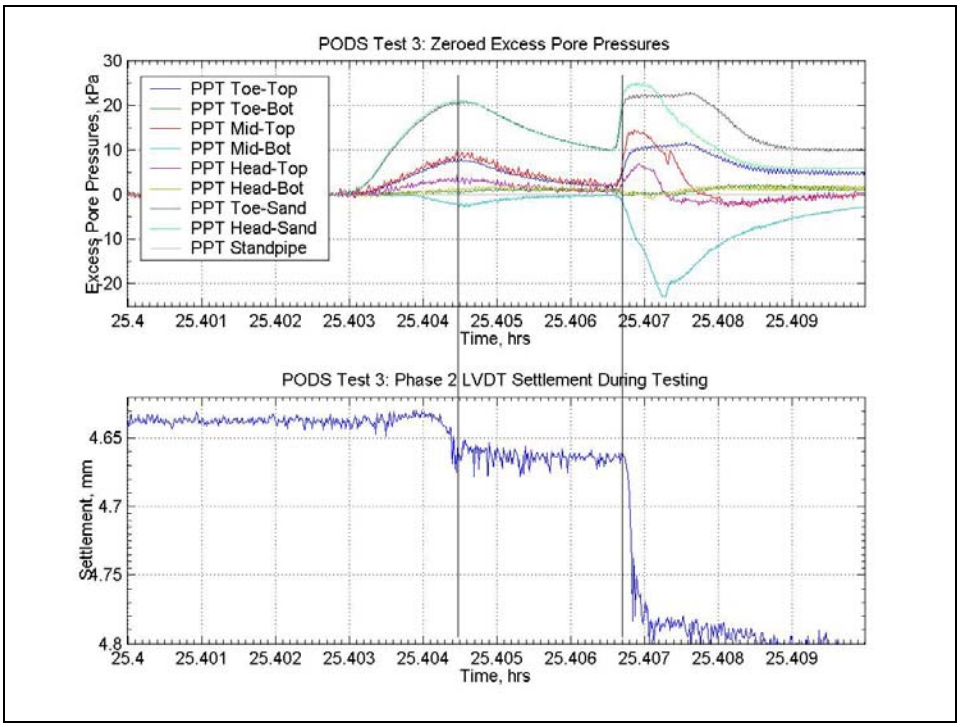

Figure 29: Test 3 LVDT displacements corresponding to excess pore pressure.

Figure 30 clearly demonstrates the spaghetti marker displacements and confirms the slope did experience failure under the applied water pressure to the sand layer. The spaghetti markers indicated that movement was located mainly at the centre of the slope, with 3-5mm of movement recorded. The limited soil movement is a function of the constraints imposed by the finite size of the box, and also the limited period of time at which high pore pressures were maintained before being released to the surface water. Little discernible movement was observed at the crest or toe of the slope. Also, there was little sign of remolding at the soil surface or any measurable change in the slope angle. Figure 31 shows more clearly the soil movement through the viewing window.

X-rays were taken of the soldered spaghetti markers as shown in Figure 32. The spaghetti strands show similar signs to those in the viewing window, with a slope failure plane along the upper clay layer and sand layer interface. There were no signs of soil displacement in the lower clay layer. Based on the failure plane shown by the markers, a postulated failure plane has been superimposed onto the model profile in Figure 33.

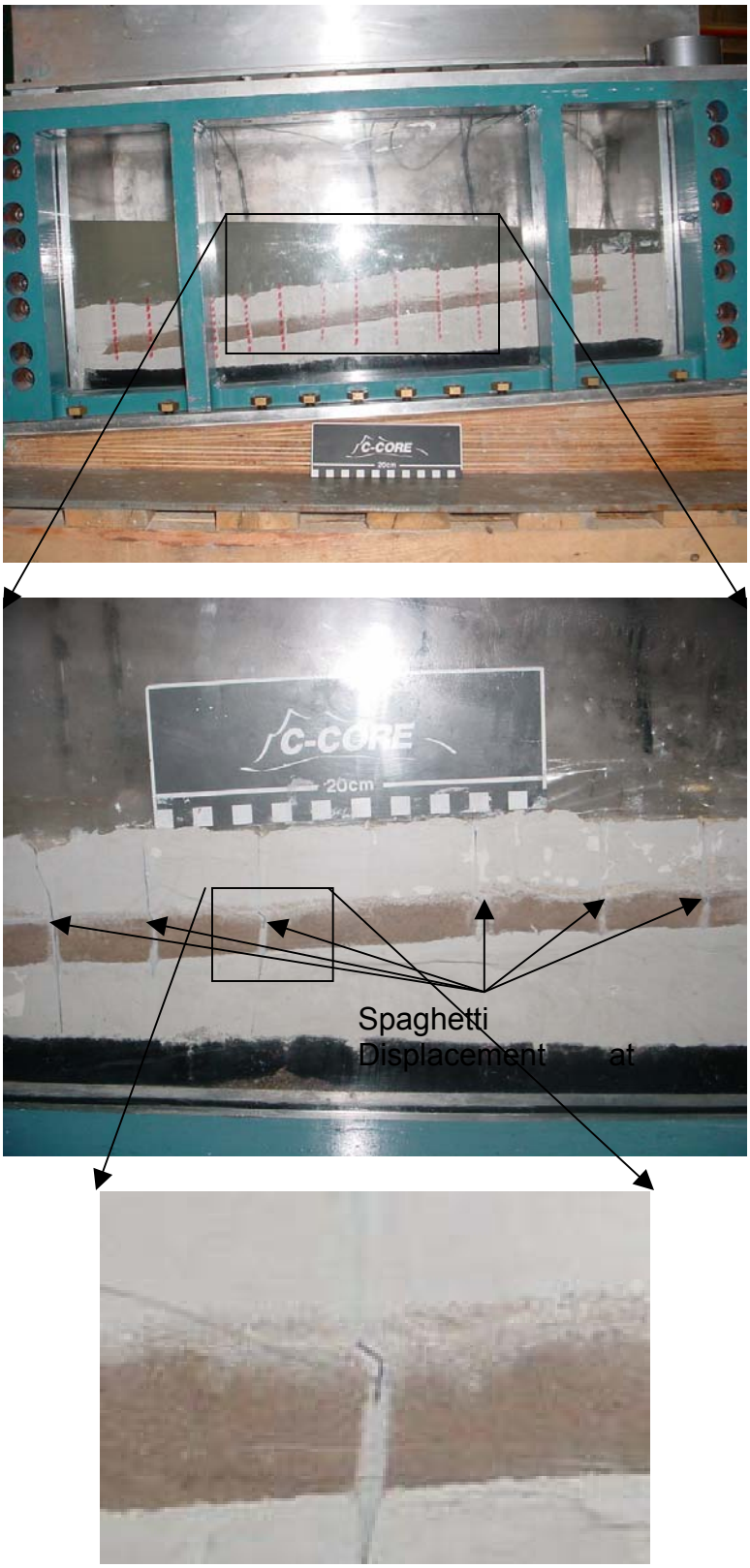

Figure 30: Observation of Slope Movement, Test 3

Figure 31: Slope Movement shown by Spaghetti Markers, Test 3

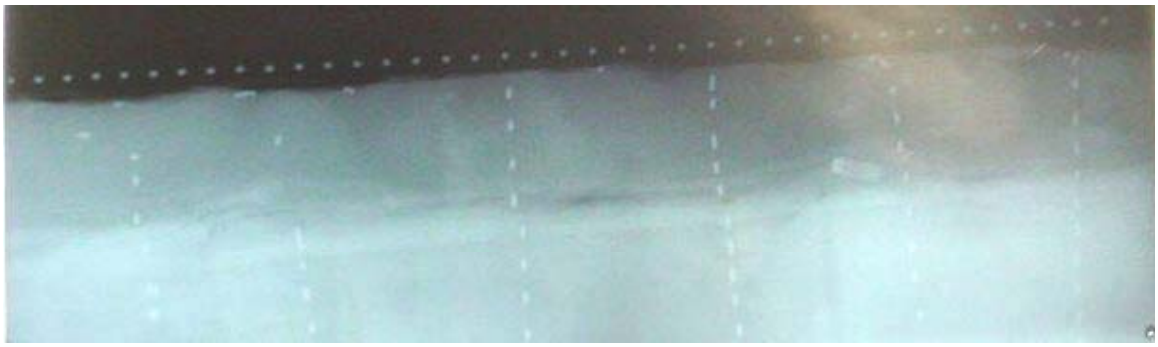

Figure 32: Test 3 x-ray images of soil after slope failure.

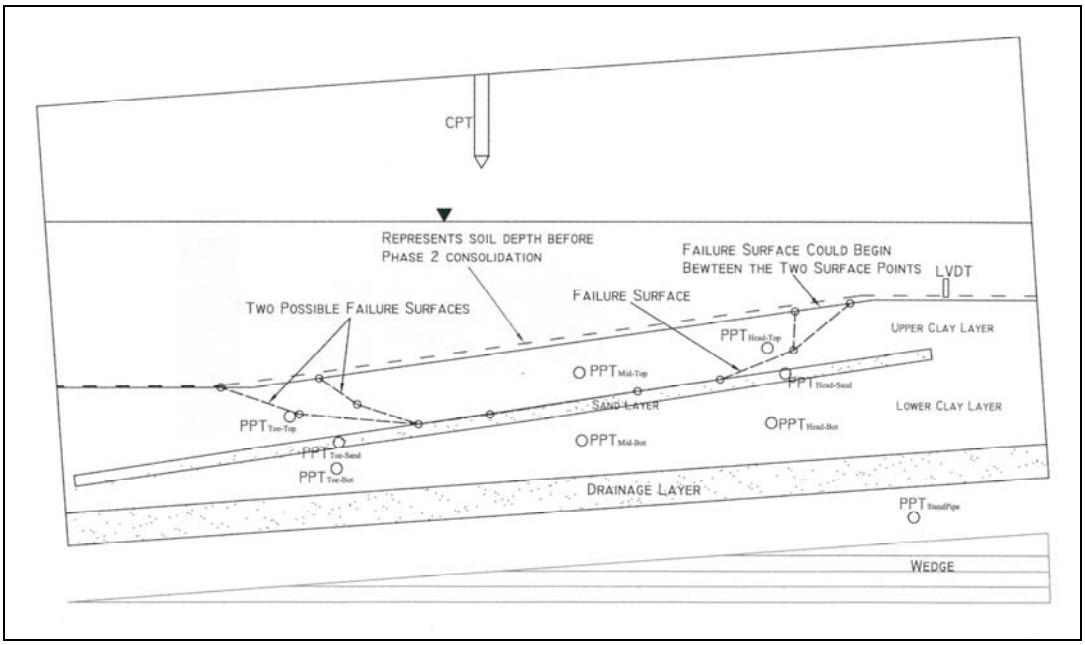

Figure 33: Test 3 profile view of phase 2 including failure plane.

Analysis of the slope was again performed using Geoslope SLOPE/W software. The sand layer was modeled with a cohesionless material with internal angle of friction of 35°. The results of two analyses are shown in Figure 34, with circular and planar slip surfaces. Both analyses calculated similar results for a given applied pore pressure in the slope. A value of pore pressure ratio, r_u, defined as the ratio of excess pore pressure (above hydrostatic) to effective overburden (u^*/σ_v') of 0.84 resulted in a calculated factor of safety of 1.094 and 1.015 respectively. This represents an excess pore pressure of 30kPa for the geometry of the slope tested in the centrifuge. This is higher than the measured value of 23 to 25kPa measured.

Analyses using an infinite slope stability model was also performed. This simplified analytical method assumes an infinite slope with no boundary conditions, with all movement being plane strain along a surface parallel to the slope. The results are meaningful for conditions large, shallow slides. Standard infinite slope stability equations for underwater slopes (Morgenstern 1967) have been developed to account for increased pore water pressure at the base of a strata, with Factor of Safety (FOS) defined as follows:

$$FOS = \tan\phi'/\tan\beta\ [1-\gamma_w/\gamma'(A-1)]$$

Where: ϕ' is the internal angle of friction of a cohesionless soil
β is the slope angle
γ_w is the unit weight of water
γ' is the effective unit weight of the soil
` A is the ratio of pore water pressure to hydrostatic values

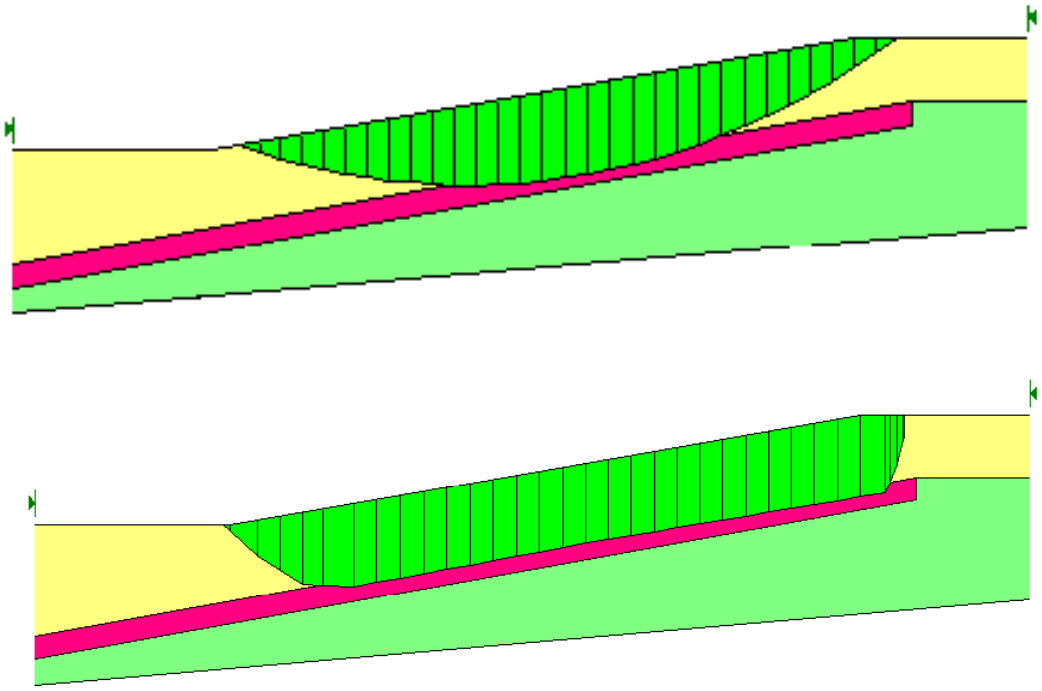

Figure 34: Analysis of Test 3 Conditions using SLOPE/W

The value of A can be related to pore pressure ratio, r_u by:

$$r_u = (u^*-u_o)/\gamma' z$$

$$A = u^*/u_o$$

$$r_u = (u^*-u^*/A)/\gamma' z$$

Where: u^* is the elevated pore water pressure referenced from seabed level
u_o is hydrostatic pore water pressure referenced from seabed level
z is the depth below seabed

The results suggest that a n excess pore pressure in the sand layer requires A values of 1.51 for ϕ' 30°, and 1.54 for ϕ' 35°, which covers the expected range for the sand used. This equates to 26 to 27 kPa excess water pressure. These values compare well with the measured values of 23 to 25 kPa, although it would be expected that this method should provide a lowerbound estimate due to the neglect of 3-dimensional boundary conditions.

Both methods of analysis showed good correlation with measured values in terms of calculation of factor of safety of these slope conditions. Care should be taken, however, in assigning slip plane parameters in limit equilibrium analyses to ensure that the correct failure mechanism is established.

2.5 Test 4 Discussion

Test 4 was performed to substantiate the results of test 3 with regard to the magnitude of the increase in pore pressures required to fail the slope. A slight modification was not to provide a distinctive toe to the slope, but rather to steepen the slope slightly at the base to reduce the effect of the strongbox boundary. The sand layer was curtailed in this area to ensure that the steepening would not influence the failure mechanism. Two additional LVDTs were also included in the test pachake to better define the soil surface movement during the test. Figures 35 and 36 show the soil cross-section of Test 4 during Phases 2 and 3 of consolidation.

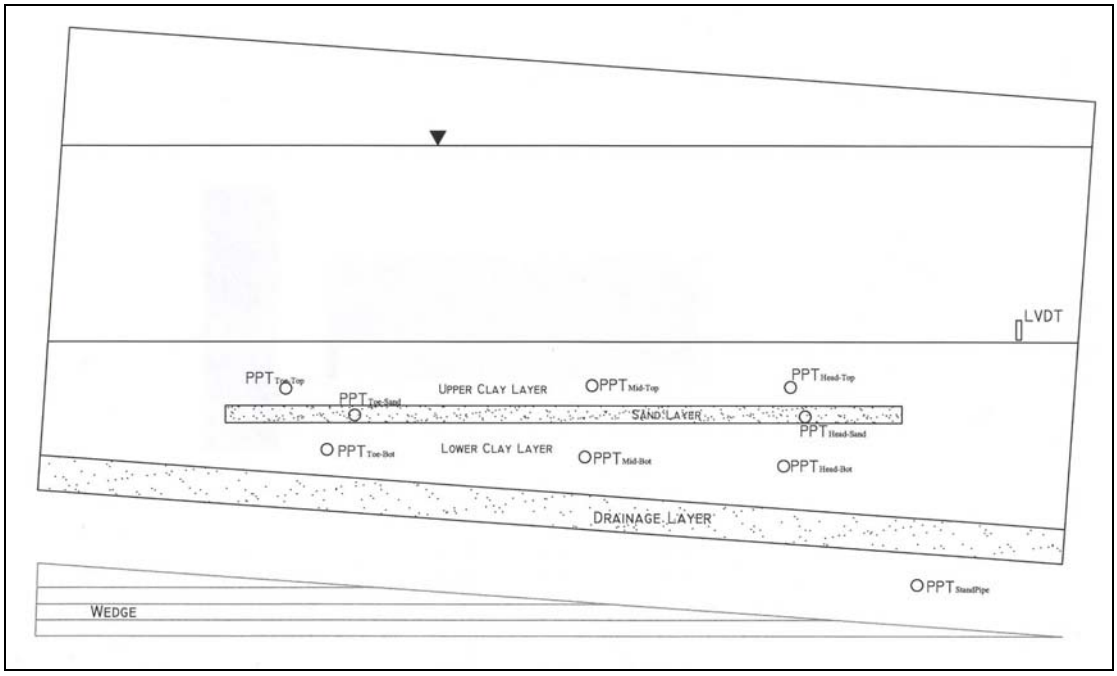

Figure 35: Test 4 profile view of phase 2 configuration.

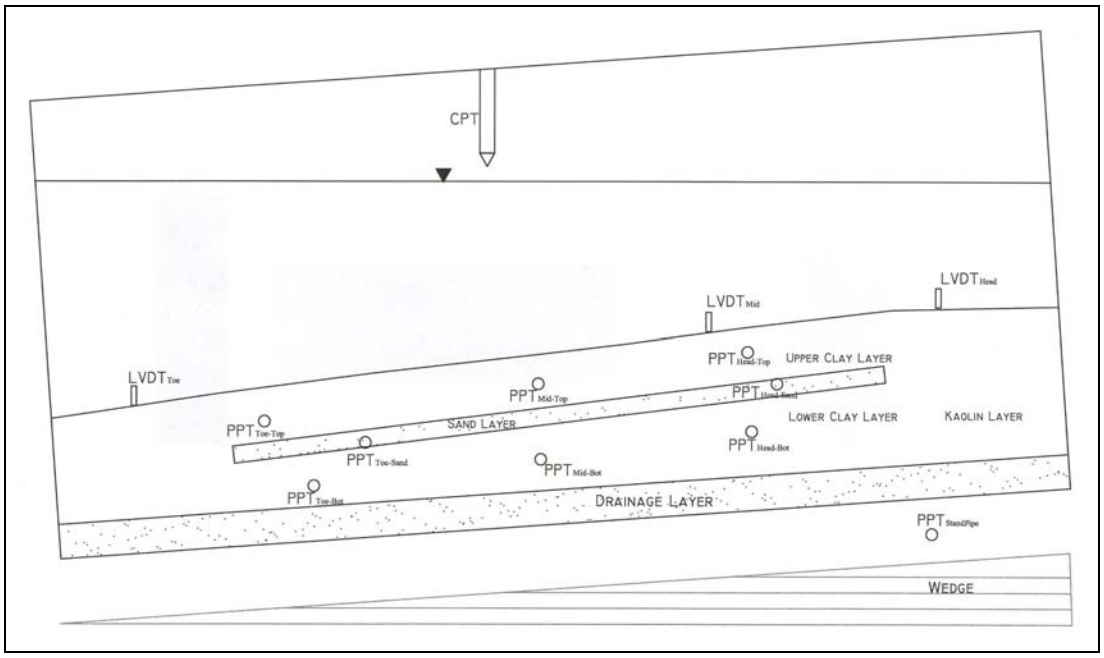

Figure 36: Test 4 profile view of phase 3 configuration.

The test procedure of Test 4 was identical to that of Test 3, with the aim of inducing slope failure by increasing the pore pressures in the sand layer. The initial height of the head leveller was positioned slightly lower than hydrostatic inside the strongbox, leading to a negative pressure as the valve was opened. This can be seen by $PPT_{Toe\text{-}Sand}$ and $PPT_{Head\text{-}Sand}$ at position A of Figure 37. The head leveller, which controlled the pressure at which water was delivered to the sand layer, was then moved upwards, as shown by the increase in pore pressures between positions A and B.

Slope failure occurred at position B, after which the head leveller was stopped and the water supply turned off at position C. It was not clear at that time whether the slope had failed since there was no clay suspension observed in the surface water to indicate flow through the overlying clay. The water was reactivated at position D and the head leveller continued upward. Almost immediately clay disturbance in the surface water was observed at position E, indicating that the pressurized water in the sand layer had short-circuited to the surface water and the pressure in the sand layer dropped.

Failure can be contributed to both injection events, which can be confirmed by Figure 38, which includes the response of the LVDTs. Initially, at position A the negative pore pressures created a small amount of displacement. The first peak of positive pore pressures at position A, there is a noticeable amount of LVDT movement, indicating slope failure. At position C, a larger settlement of up to 1mm demonstrated by the $LVDT_{Mid}$, corresponds with the second peak of positive pore pressures. $LVDT_{toe}$ showed a slight rise in level after the first event.

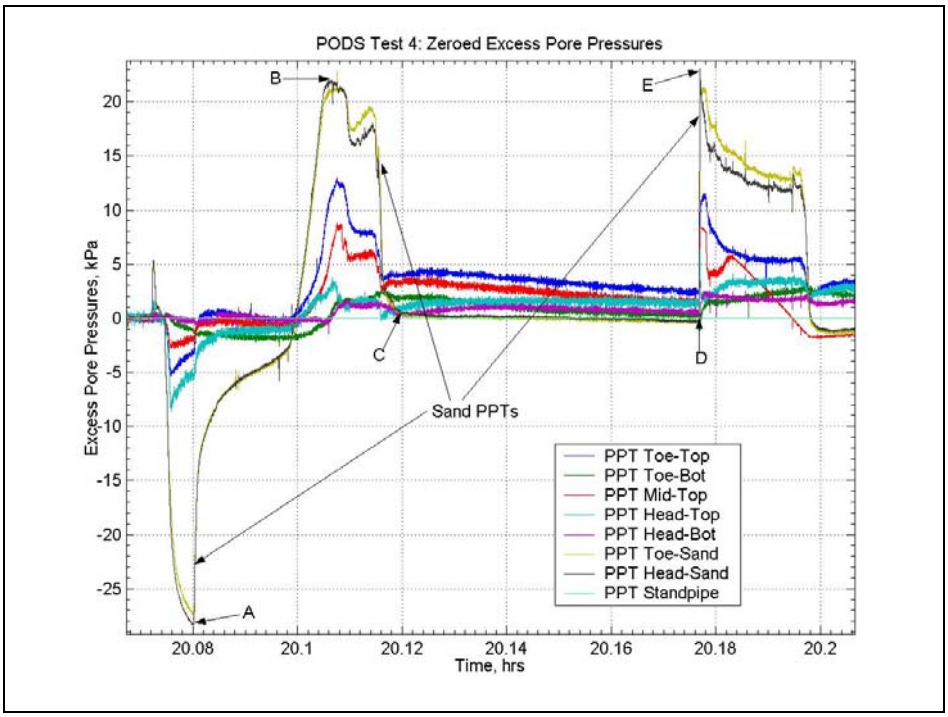

Figure 37: Zeroed excess pore pressures during test 4.

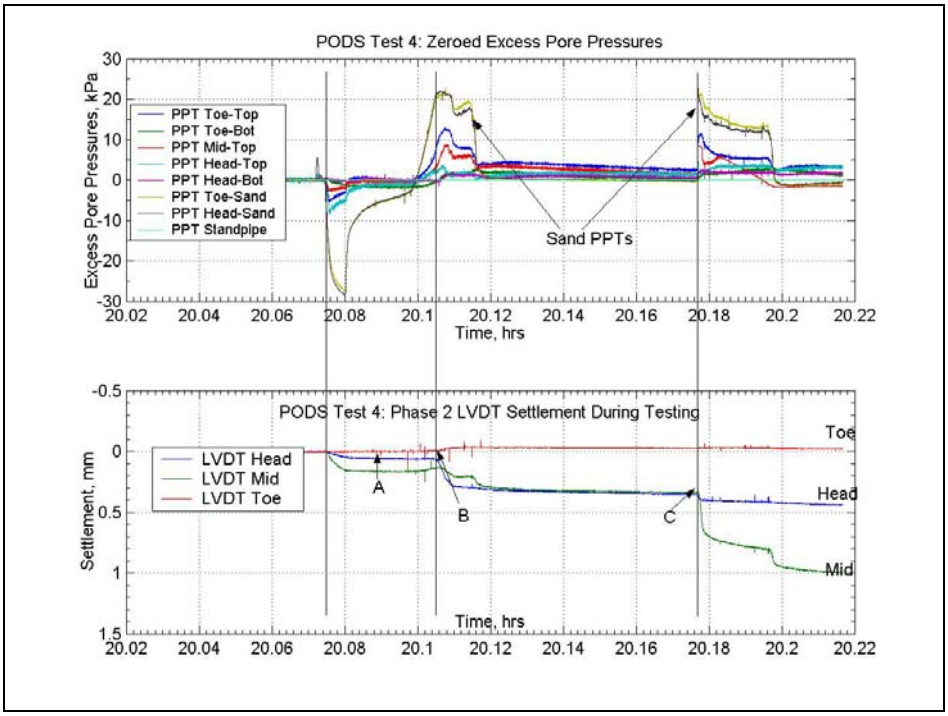

Figure 38: Test 4 LVDT displacements corresponding to excess pore pressures.

Figure 39 demonstrates the spaghetti marker displacements and confirms the slope did experience some form of lateral movement. As in Test 3, the slope failure was characterized planar slip plane along the top of the sand layer, with greatest movement near the centre of the slope. Smaller movements were observed at the crest and toe. Also similar to Test 3, there was little sign of soil accumulation at the base or significant changes of slope angle. To visually assist the original and post-failure positions of the spaghetti markers are highlighted in Figure 39.

X-rays were taken of the soldered spaghetti markers as shown in Figure 40. The failure plane is very similar that observed in Test 3. The spaghetti markers show a discontinuity at the sand/clay interface. There were no signs of soil displacement in the lower clay layer. Based on the failure plane observed in the x-rays, a failure plane was imposed onto the model profile in Figure 41.

The magnitude of the pore pressures achieved in the sand layer were almost identical to those measured in Test 3, reaching 22 to 23 kPa. The thickness of the overlying clay layer was the same as in Test 3, and the measured slope movement and shape was similar in both cases.

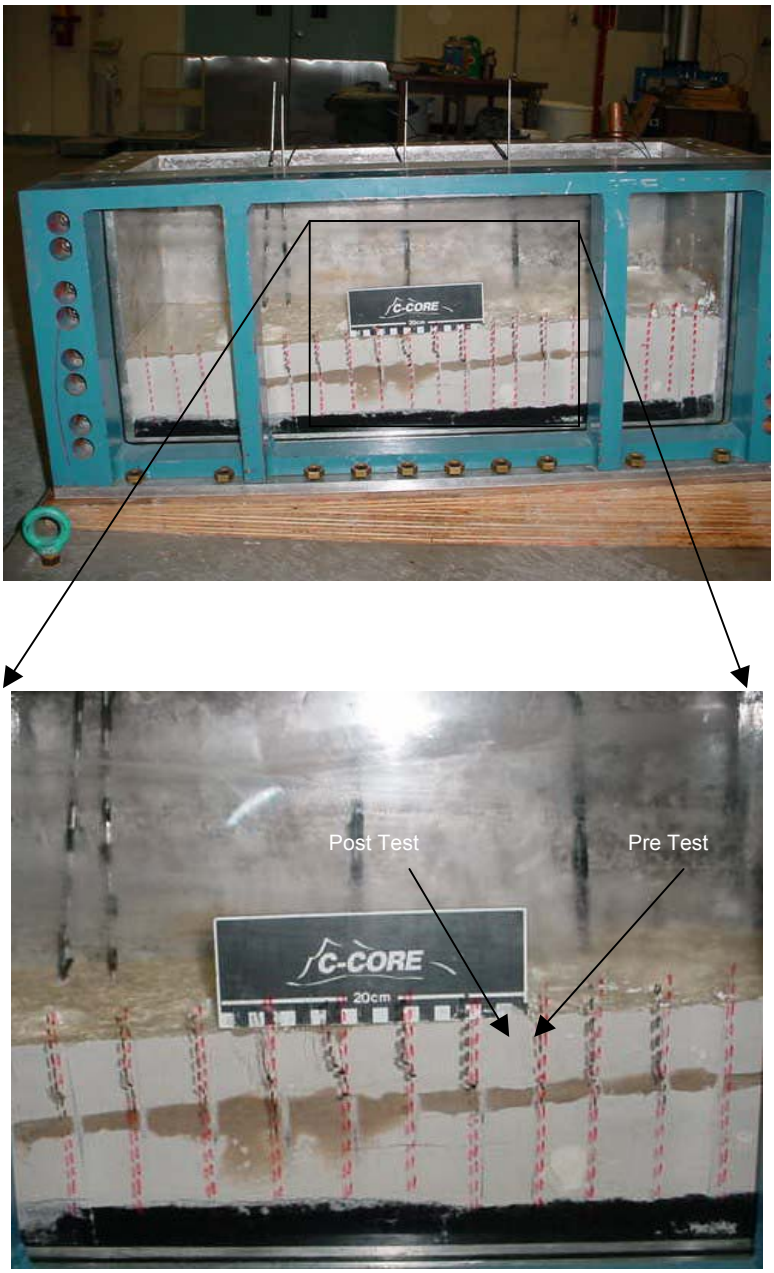

Figure 39: Observation of Slope Movement, Test 4.

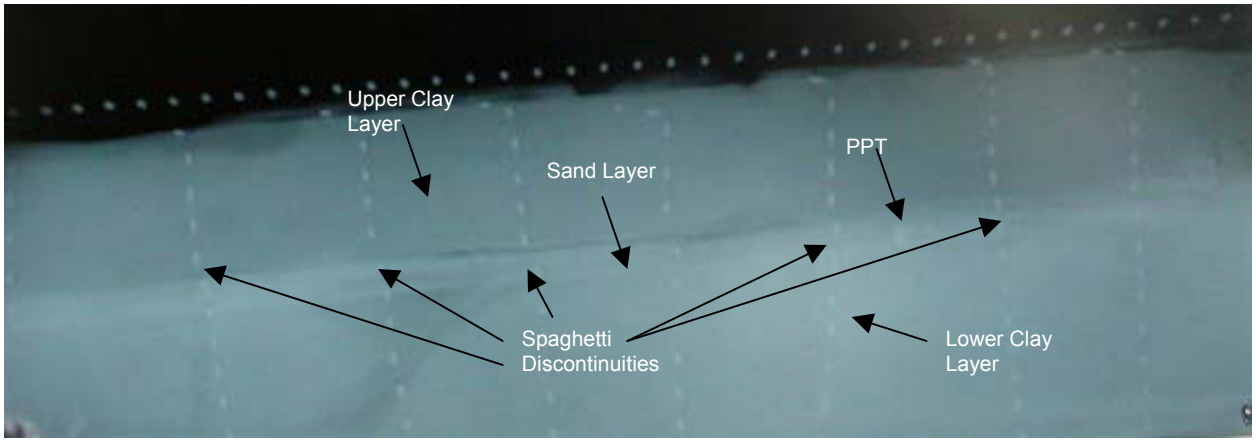

Figure 40: Test 4 x-ray images of soil after slope failure.

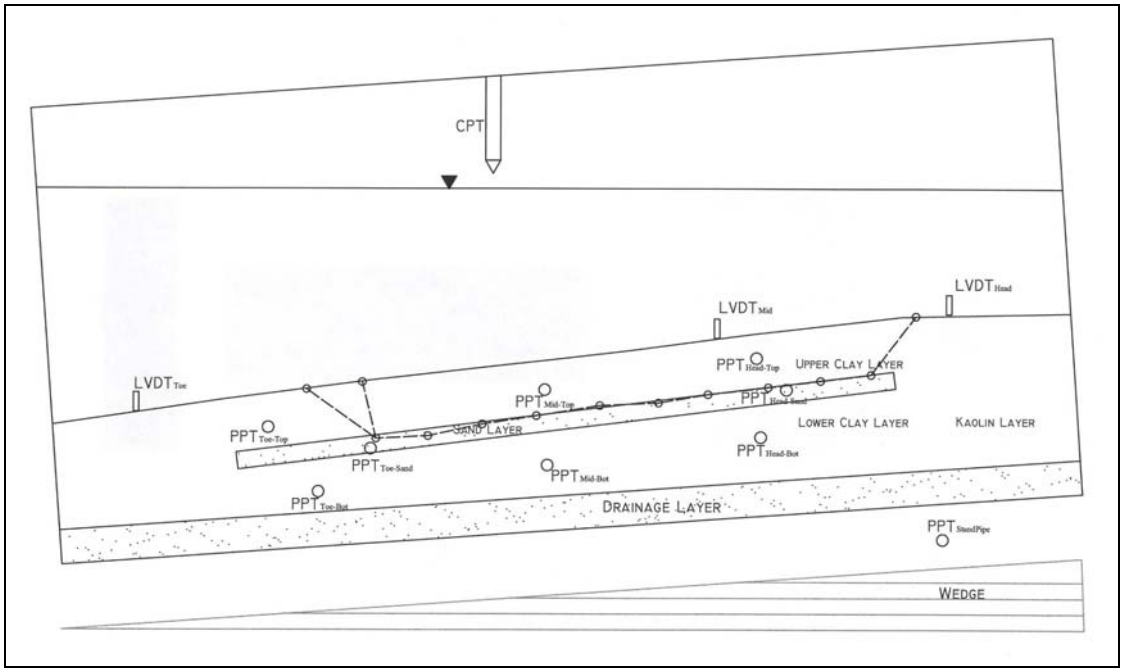

Figure 41: Test 4 profile view of phase 2 including failure plane.

3.0 GAS HYDRATES

Jocelyn Grozic at the University of Calgary has been contracted to perform analyses on the effects of gas hydrates on underwater slope stability. The scope includes evaluation of the geomechanical behaviour of hydrate/sediment mixtures and the effects of dissociation on the surrounding soil and impact on slope stability. The University of Calgary is in the process of establishing a physical testing laboratory focusing on the geotechnical properties of gas hydrates, which will be invaluable in providing an advanced understanding of the processes involved and in developing a model of hydrate behaviour during dissociation.

An initial report has been prepared and is included in Appendix A. The report discusses the properties of gas hydrates, their formation and dissociation and occurrence. The potential effect of gas hydrates on slope stability is discussed and a number of case studies investigated where there is evidence that gas hydrates may have had an influence. Research into gas hydrates is at an early stage in comparison with most other materials and processes, and so the starting point for this task of the PODS project was at a much more fundamental level.

It is noted that fundamental research is needed in order to be able to apply knowledge on gas hydrates in practical situations. In particular, better knowledge of behavioural properties and processes, dynamic equilibrium and the effect of perturbations on stability, and the ability to detect in-situ presence and distribution are highlighted as requirements that can lead to integration with engineering assessments of slope instability.

The gas hydtrates research is ongoing as part of PODS Phase 2 with the objective of answering some of the questions raised as part of the literature study. This will include the development of a geomechanical model of gas hydrate behaviour, which considers the physical effects of dissociation on the surrounding soil. Integration of this model into deterministic slope stability analytical methods is expected as part of this project.

4.0 RISK ANALYSIS FRAMEWORK

This part of the study focuses on the development of methodologies for determining the probability of failure of a slope based on a range of input parameters. The conditions found on the Scotian Slope are being used as a basis for developing this work, but the general methodology will eventually be applicable to any area on a regional basis.

This section outlines the methodology developed for risk analysis of submarine slope failure. The methodology employs a probabilistic approach, which accounts for uncertainty in slope failure mechanisms as well as loading events (triggering agent).

The developed methodology has been used to generate regional hazard maps of slope failure on the Scotian Shelf using available data for site conditions and releasing agents. This report describes the generation of hazard maps that specifically consider the inertial effects of earthquake events. The produced maps are presented for demonstration purposes as more detailed work and data are required to produce realistic hazard maps. The methodology can be extended to other trigger events and failure mechanisms, and applied to smaller site specific locations, where a greater level of geotechnical and environmental data can be collected.

The Geological Survey of Canada (Atlantic) (GSC) has prepared a report providing geotechnical, geophysical and geological interpretation of the conditions on the Scotian Slope. The work includes an assessment of the available parameters that may be input into a risk-based study, including maps of slope angles, dominant soil types and strength, geological activity, previous failure events, historical earthquake activity etc. This information is then analysed to provide a probabilistic assessment linking existing conditions to potential triggering mechanisms. The GSC report is included in Appendix B.

4.1 Scotian Shelf – Site Conditions

The PODS Phase 1 report (C-CORE, 2002) presented site parameters and general characterization of the Scotian Shelf. This has been followed up in the GSC report, which provides additional data, including discussion on the collection and interpretation of the data.

Bathymetry data

The regional bathymetric were generated on 500m by 500m grid using publicly available depth sounding bathymetry data. The regional bathymetric grid was used to calculate slope angles on a resolution of 500m by 500m. More accurate bathymetric data on grid of 22m by 22m was available using multi-beam systems for specific areas. These data sets are proprietary and are not available for direct use as part of this project, although they offered a correlation with the coarser data grid. Slope angles were compared between the two data sources to allow potential error sources to be identified. GSC recommended the following correction for slope angles obtained on the coarse data:

$$\Delta = \beta - \beta_f$$

$$\Delta = -0.787\beta_f + 2.401$$

where β is slope angles obtained from coarse bathymetric data (coarse slope); β_f is slope angles obtained from fine resolution bathymetric data; and Δ is the difference. Substituting for Δ, the corrected slope angle from coarse slope is:

$$\beta_c = 4.695\beta - 11.28$$

where β_c is the corrected slope angle. The data showed a strong correlation between slope angle and error between the two sources. This is logical, as the coarser data set would be expected to miss the finer details in relatively rugged terrain as a function of averaging over a 500m square. Gentle slopes (<2 degrees) are an exception to the above correlation and so it is considered reasonable to limit application of the correlation to slope angles greater than 2^o.

In summary, publicly available coarse slope angles may not be suitable for a real engineering problem. Figure 42 shows corrected coarse slope angles for Scotian Shelf (for the area west of 59°); the correction is not applied for slope angles smaller than 2 degrees.

Figure 43 shows locations of shallow geotechnical cores. The locations at which, values of undrained shear strength (using laboratory vane shear test) and density were measured are given and summarized in Table 2. The data is limited to the depth of the cores, generally less than 10m.

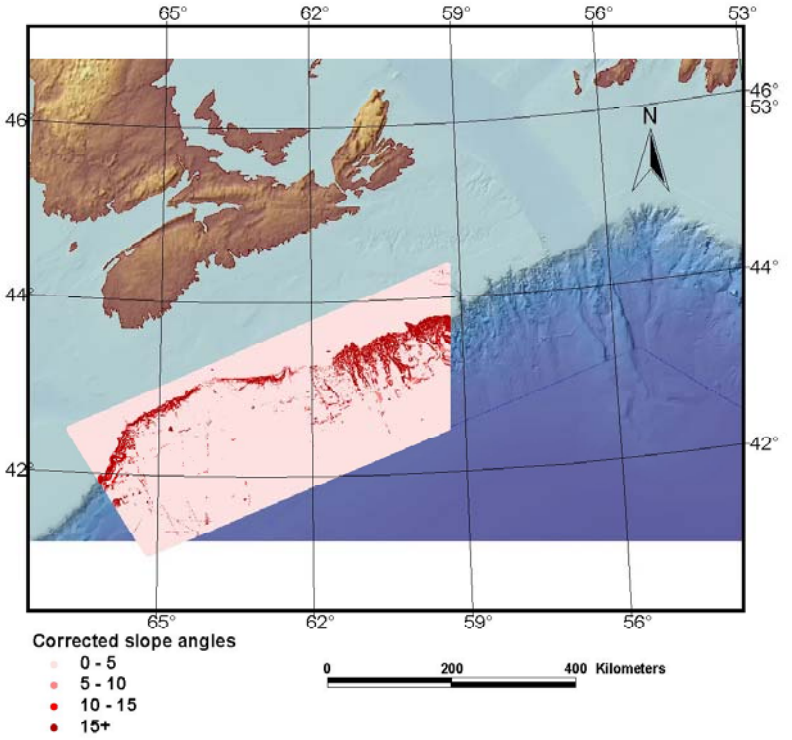

Figure 42: Corrected Slope Angle on the Scotian Slope

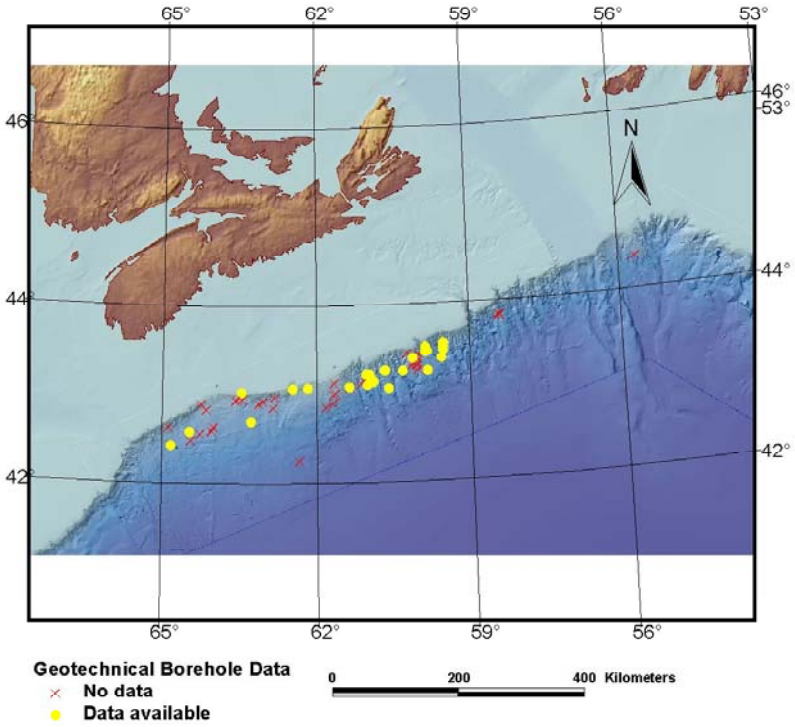

Figure 43: Location of geotechnical cores

4.2 Methodology

The methodology, presented here, illustrates how it is possible to integrate topographic, geotechnical and environmental data in one database and use them in performing risk analyses for submarine slope failures. The presented results are for demonstration purposes due to limitation of available data. The methodology presented in this section will be further developed to allow evaluation of better-defined locations where a higher density of data is available.

Engineers and geoscientists have established various methods to produce landslide hazard maps. Landslide hazard maps were produced using historical records, geological conditions, topography, geotechnical analysis etc. Geographic Information System (GIS) and associated software packages have significantly enhanced processing of spatial data and provided necessary tools to integrate various information sources in recent decades. Jibson et al. (1998 & 2000), Wu and Abdel_Latif, 2000 and Zhou et al. (2003) established and applied different methodologies that combine GIS information and probabilistic concepts to produce slope failure hazard maps. In recent decades, many researchers have used probabilistic approaches to perform risk analysis for slope failure and evaluate slope stability reliability (e.g. Tang et al. 1976; Christian et al 1994; Christian and Urzua 1998; El-Ramly et al. 2002; and Nadim et al. 2003).

One of the major hazards in many areas is the consequence of earthquake events. The eastern seaboard of Canada is a seismically active region, with earthquakes recorded on a regular basis. The effects of earthquakes on slope instability were clearly demonstrated in 1929 when a magnitude 7.2 earthquake caused failure of a large area of the St Pierre Slope, south of Newfoundland. Up to 150km^3 of seabed was mobilized during the event, and the resulting tsunami caused widespread destruction on the nearby Burin Peninsula in Newfoundland. An analysis of the slope failure was presented in the PODS Phase 1 report (C-CORE, 2002).

Figure 44 shows the proposed methodology for determination of the inertial effects of earthquake events. The approach is similar to that used by Jibson et al. (1998 & 2000), modified to address the particular issues of interest. The methodology uses:

Digital Elevation Maps (DEM), which were produced from GIS information, to evaluate slope angle at each grid point
Geotechnical data to evaluate soil shear strength at each location
Earthquake information sources to define zones of same earthquake risk and construct the associated hazard curve for each zone

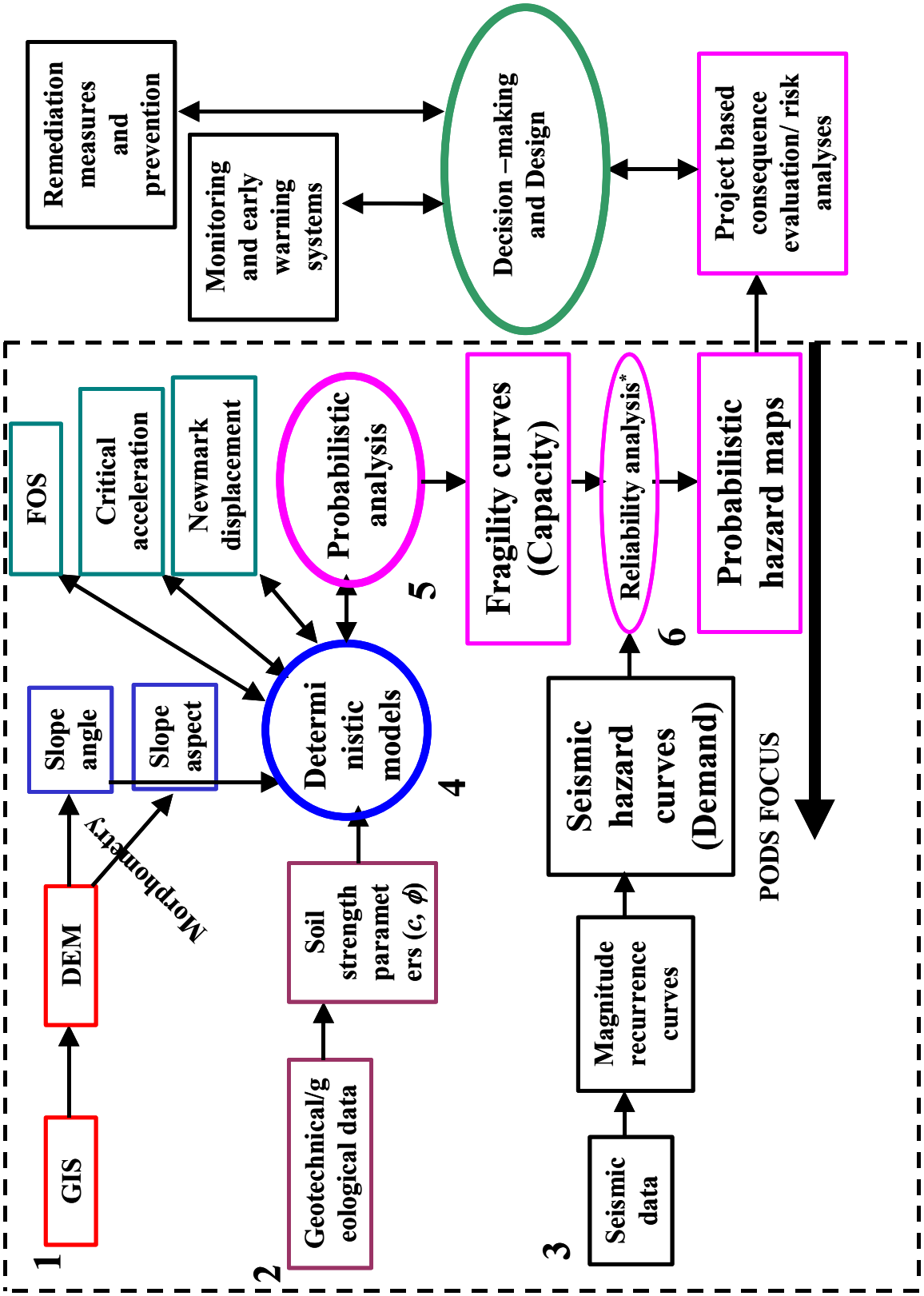

Figure 44: Proposed Methodology for Risk Analysis

4.3 Deterministic Model

Morgenstern (1967) presented a simple pseudostatic mechanical model, based on finite slope assumption, for earthquake loading. This model is selected as the starting point of the deterministic model. For an infinite slope with a soil of increasing shear strength with depth, the factor of safety is given by:

$$FS = \frac{2c_u}{\sigma'_v \sin\beta}$$

where c_u/σ'_v is the ratio of undrained shear strength to effective vertical stress. Accounting for earthquake horizontal acceleration, a_h:

$$FS = \frac{c_u}{\sigma'_v\left(0.5\sin\beta + a_h \frac{\gamma}{\gamma'}\cos^2\beta\right)}$$

The above equation can be rewritten to define critical acceleration. Critical acceleration is the acceleration that initiates failure (or yield acceleration, i.e. FS<1)

$$a_{crit} = \frac{\frac{c_u}{\sigma'_v} - 0.5\sin\beta}{\frac{\gamma}{\gamma'}\cos^2\beta}$$

As an alternative method to the above pseudostatic method, the Newmark method (Newmark, 1965) can be used. The pseudostatic method does not provide any information about soil deformation after yield (FS<1) and postulates failure for FS<1. Newmark considered that soil mass will be accelerated when it is not in equilibrium (i.e. FS<1), resulting in permanent deformation. The solution calculates slope displacements by integrating earthquake time history for accelerations exceeding the critical acceleration (Kramer, 1996).

Quantification of following parameters is required for the both approaches:

- Ratio of soil undrained shear strength to vertical stress, $sr = \frac{c_u}{\sigma'_v}$
- Slope angle, β
- Horizontal earthquake acceleration, a_h

A deterministic analysis requires best estimates of the above parameters, while the parameters are treated as random variables rather than constant values in a probabilistic analysis. Uncertainty associated with each parameter should be quantified for reliability analysis.

4.4 Slope Stability – Probabilistic Analysis

For probabilistic analysis, we need to define the limit state(s) or the performance function(s). An obvious limit state in the pseudostatic method is $FS < 1$. Thus, the performance function is:

$$G(X) = FS\text{-}1$$

Probability of failure can be calculated using:

$$p_f = \int_{G(X)<0} F(X)dX$$

where p_f is the probability of failure; X is the parameter of performance function; $F(X)$ is joint probability distribution of X. In structural analysis, load and resistance are often separated. However, this may not possible in many geotechnical applications due to interdependence of load and resistance. It is common in earthquake engineering to express probability distribution of loading and resistance as hazard and fragility curve.

Hazard and Fragility Curves

Hazard curves define a measure of ground motion intensity, e.g. Peak Ground Acceleration (PGA), as a function of probability level. Hazard curves are constructed based on earthquake inventory and geological conditions for each region. Seismic hazard maps and hazard curves can be developed using the Cornell-McGuire method as described by Cornell (1968) and McGuire (1977). The method defines zones of same seismic intensity and assumes that earthquakes are randomly distributed in time and space within that region. Atkinson et al. (1987), Adams and Halchuk (2003) and Adams and Atkinson (2003) discussed development of seismic hazard maps and hazard curves for Canada and the Eastern Canadian Offshore Regions. Figures 45 and 46 show examples of earthquake source zone maps of Canada. Figure 47 shows examples of hazard curves for Canadian cities.

The fragility curve for a limit state is the cumulative probability of exceeding that limit state for a given value of ground motion intensity (cumulative probability of failure). The fragility curve characterizes the probabilistic distribution of the system stability (resistance) for a given limit state. Figure 48 shows a typical hazard and fragility curve. Fragility curve is essentially the cumulative probability distribution of resistance.

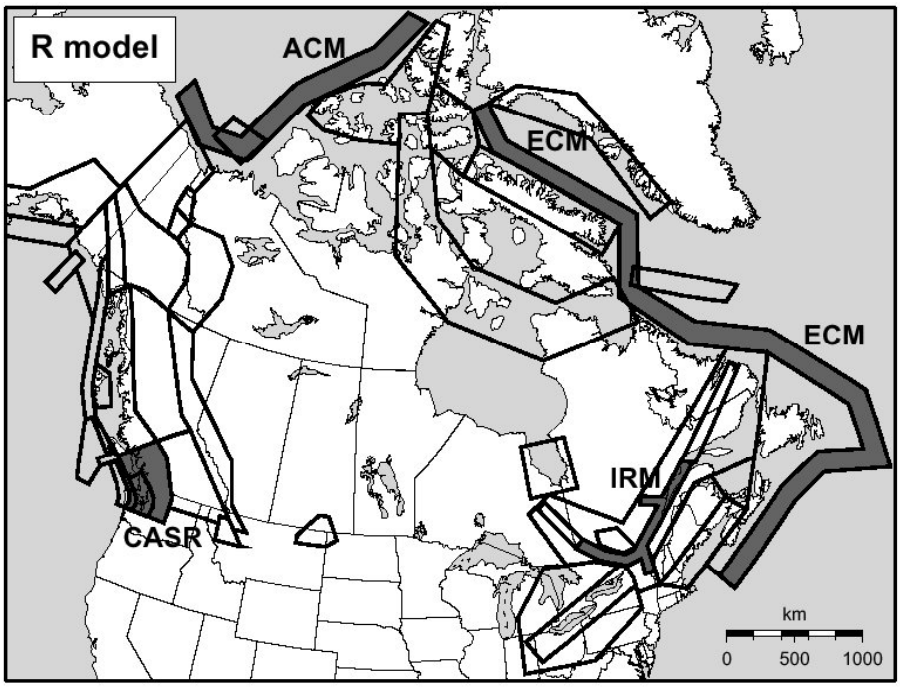

Figure 45: Earthquake source zone maps of Canada – R-model (after Adams and Atkinson, 2003)

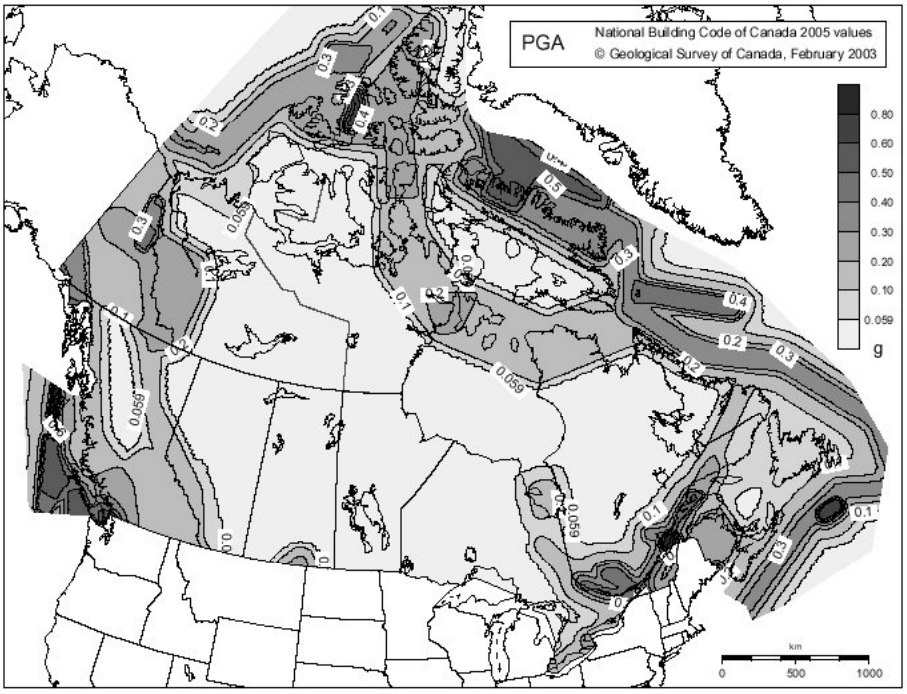

Figure 46: Median values of PGA at probability level of 2% in 50 years for Canada (after Adams and Atkinson, 2003)

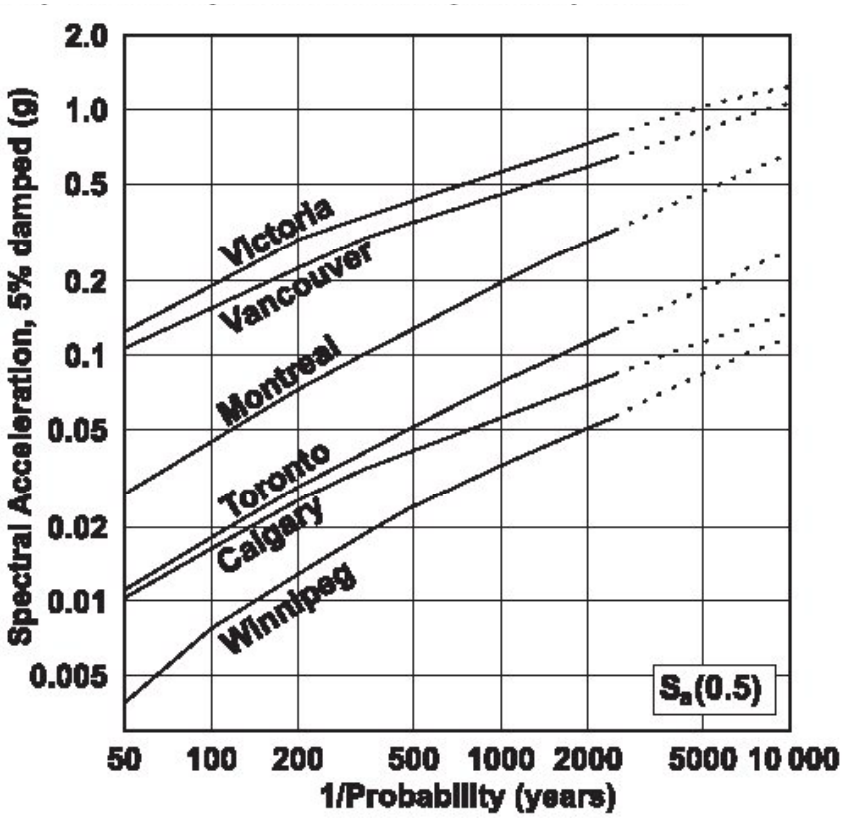

Figure 47: Hazard curves for selected Canadian cities (after Adams and Atkinson, 2003)

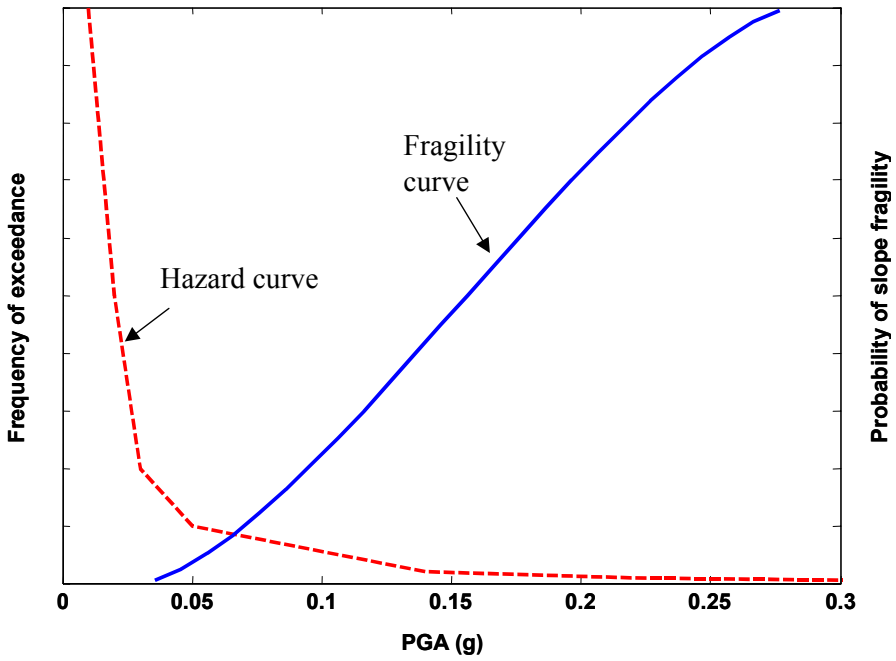

Figure 48: Sketch of hazard and fragility curve

There are various sources of uncertainty in geotechnical engineering. Measured soil properties show significant variability from point to point. Researchers presented different classifications for uncertainty in engineering problems. For example, Christian et al. 1994, Phoon and Kulhawy (1999a) and Nadim et al. 2003 presented a few examples of classifications for uncertainty in geotechnical engineering. In general, there are two main type of uncertainty

- Aleatory uncertainty: Representing natural randomness such as natural variability soil properties in vertical and horizontal layers or variation in the peak acceleration of an earthquake

- Epistemic uncertainty: Representing the lack of knowledge such as measurement or statistical uncertainty or model uncertainty. These can generally be reduced by obtaining more data, or by validation of model performance.

Phoon and Kulhawy (1999a) classified the inherent variability, the measurement errors, and the transformation uncertainty as primary sources of geotechnical uncertainty. Tang (1984) and Phoon and Kulhawy (1999b) established simple methodologies to analyze the effects of these individual uncertainties. Nobahar (2003) discussed various sources of uncertainty and presented an application of such an approach to account for different sources of uncertainty.

4.5 Numerical Exercise

The methodology for determining the annual probability of earthquake induced inertial failure has been demonstrated for Scotian Slope conditions.

Only one earthquake zone is assumed for the contoured area shown in Figure 42 (west of 59°). Based on Adams and Halchuk (2003), Adams and Atkinson (2003) and J. Adams (2004), the hazard curve shown in Figure 49 was constructed. The values of peak ground acceleration and corresponding probability are taken from the R-model for the ECM zone and extrapolated for lower return periods.

To assess probabilistic characteristics of slope stability (i.e. to build the fragility curve), a range of different sources of uncertainty need to be addressed, including natural soil variability, statistical errors, bias, model uncertainty etc. However, the region analyzed in this case is too vast and data is too limited to perform a detailed and reliable analysis. A simplified approach is therefore used to evaluate uncertainty associated with slope stability (resistance).

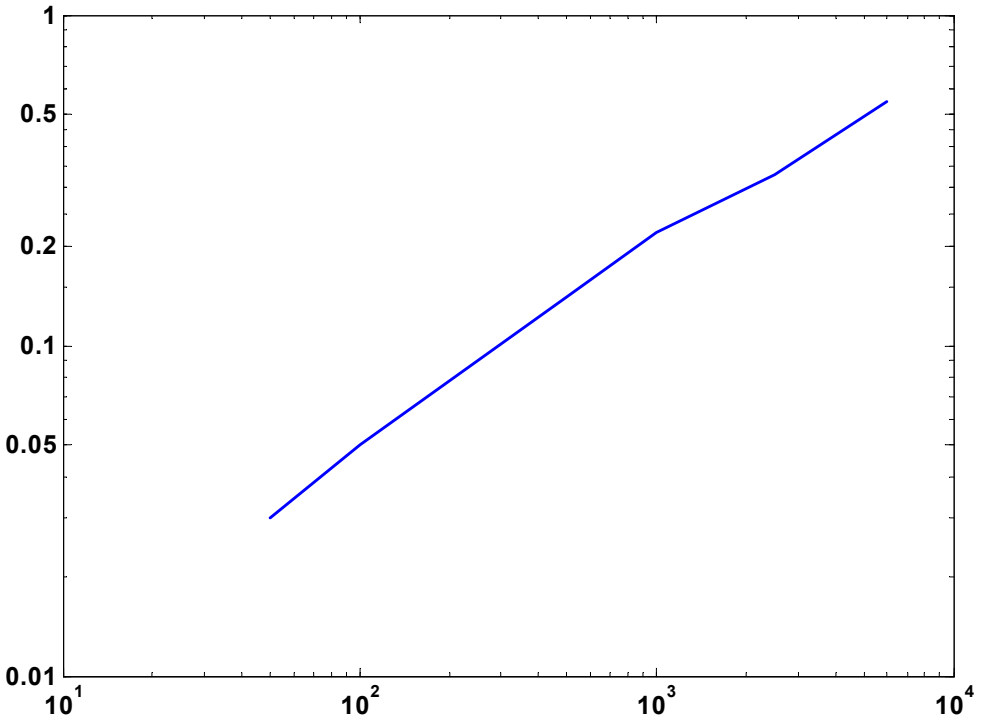

Figure 49: Hazard Curve Generated for the Scotian Slope

Figure 50 shows the soil strength profiles obtained from a number of cores in the area west of 59° and east 62°. The soil strength profiles show generally increasing strength with depth, covering a range of ratios of undrained shear strength to vertical stress, *sr*, in the top few meters. The dashed black lines show the range in values of *sr* from 0.1 to 0.35, which covers the values normally attributed to normally consolidated clay soils. Table 2 tabulates the estimated values for the characteristic or design value (sr_c), average value (sr_a) and standard deviation (std). Average values of *sr* are calculated by averaging soil undrained shear strength ratio omitting the effects of the crust in the top 2 meters.

Figure 51 shows the probability distribution of design values of *sr*. This distribution has been assumed to be representative of conditions over the whole area being considered. Thus, variability of soil strength from different boreholes can be treated as uncertainty in estimation of soil characteristic strength. A symmetric Beta distribution with parameters a = b = 1.5 fits well to Figure 52 shows the distribution of sr_a. An exponential distribution has been found to fit sr_a.

Table 2: Soil strength parameters from geotechnical boreholes

Geographical location						Soil strength ratio, *sr*		
Geographic area	Latitude	Longitude	Depth (cm)	Slope Angle	Water Depth (m)	design	average	std
North Atlantic Ocean - Slope off of Emerald Bank	42.87	-62.46	440	4.3187	818	0.15	0.179	0.053
North Atlantic Ocean - Slope off of Emerald Bank	42.88	-62.16	809	7.5689	680	0.300	0.416	0.100
North Atlantic Ocean - Slope off of Western Sable Island Bank	43.11	-60.64	301	5.6437	1664	0.198	0.198	0.050
North Atlantic Ocean - Slope off of Western Sable Island Bank	43.12	-60.65	660	8.2486	1505	0.313	0.313	0.110
North Atlantic Ocean - Logan Canyon area	43.10	-59.82	NA	NA	2253	0.300	0.376	0.252
North Atlantic Ocean - Logan Canyon area	43.28	-59.55	480	5.7547	2414	0.200	0.250	0.086
North Atlantic Ocean - Logan Canyon area	43.39	-59.50	875	9.2299	1853	0.250	0.300	0.128
North Atlantic Ocean - Logan Canyon area	43.38	-59.82	468	9.2567	1778	0.330	0.665	0.276
Scotian Shelf -	43.45	-59.50	190	1.0128	1735	0.200	0.293	0.090
Scotian Shelf -	43.49	-59.50	580	3.9491	1422	0.16	0.185	0.042
Scotian Shelf -	43.37	-59.87	340	6.7255	1673	0.28	0.287	0.037
Scotian Shelf - Logan Canyon	43.44	-59.86	516	25.5684	1104	0.3	0.428	0.157
Scotian Shelf -	43.29	-60.10	730	4.7932	1360	0.2	0.222	0.095
Scotian Shelf -	43.10	-60.31	290	6.0753	2107	0.2	0.257	0.047
Scotian Shelf -	43.06	-60.96	923	3.5405	1315	0.18	0.193	0.041
Scotian Shelf -	43.06	-61.02	830	6.574	1426	0.22	0.295	0.085
Scotian Shelf -	42.96	-60.87	830	1.0128	1975	0.15	0.214	0.079
Scotian Shelf -	42.89	-61.34	212	1.601	1705	0.1	0.182	0.070
South Brown's Bank	42.25	-64.45	716	0.7035	1864	0.15	0.179	0.038
Northeast Channel	41.88	-65.62	801	6.0099	783	0.2	0.235	0.081
West Western Bank	42.92	-61.00	770	7.0719	2162	0.2	0.262	0.068
Weymouth Block	42.86	-60.58	980	4.1687	2390	0.12	0.176	0.049
Scotian Shelf -	42.06	-64.80	440	0.3815	NA	0.32	0.388	0.076
Scotian Shelf -	42.39	-63.26	340	1.1084	NA	0.4	0.519	0.111

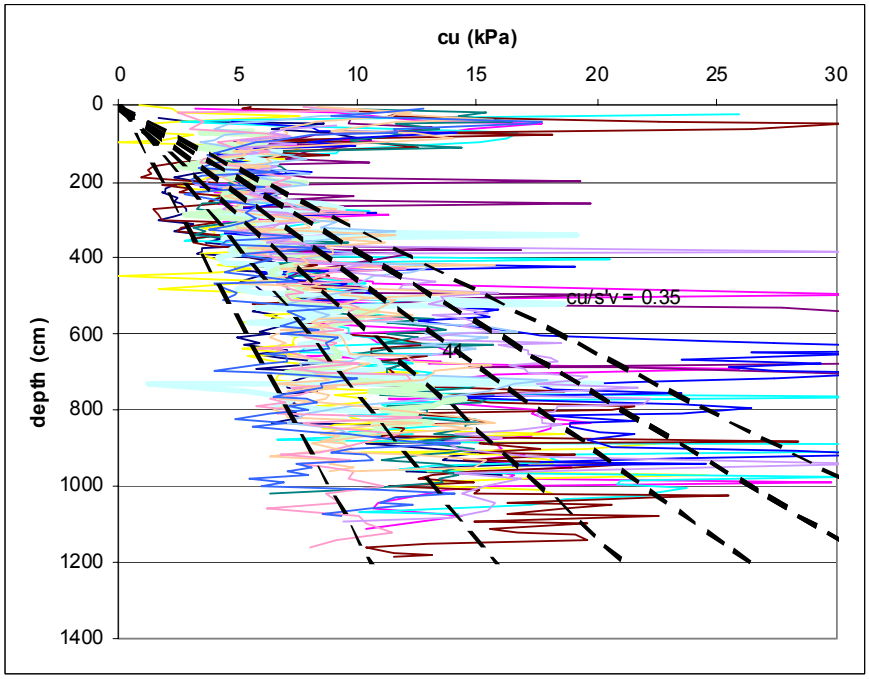

Figure 50: Soil strength profiles for geotechnical boreholes between west of 59° and east 62°

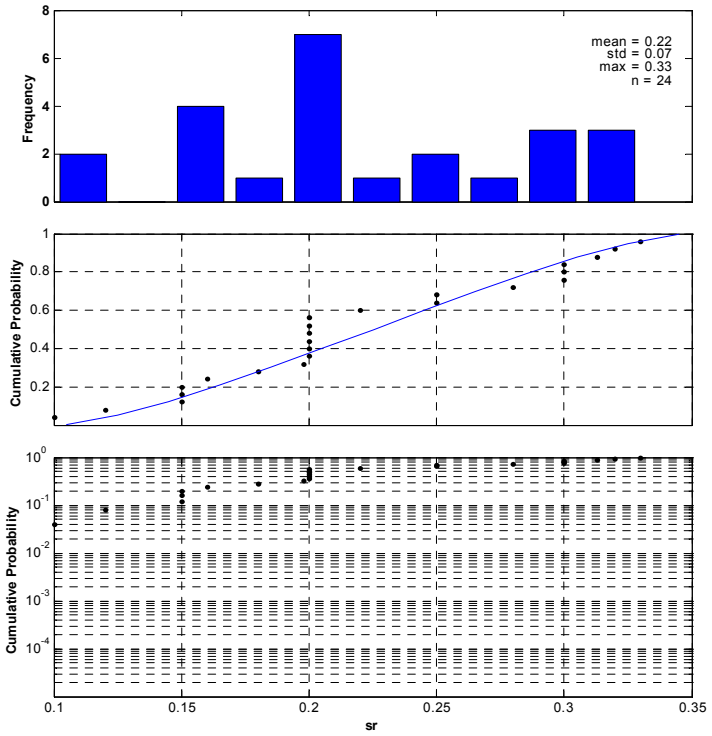

Figure 51: Probability distribution of sr_c and fitted Beta distribution

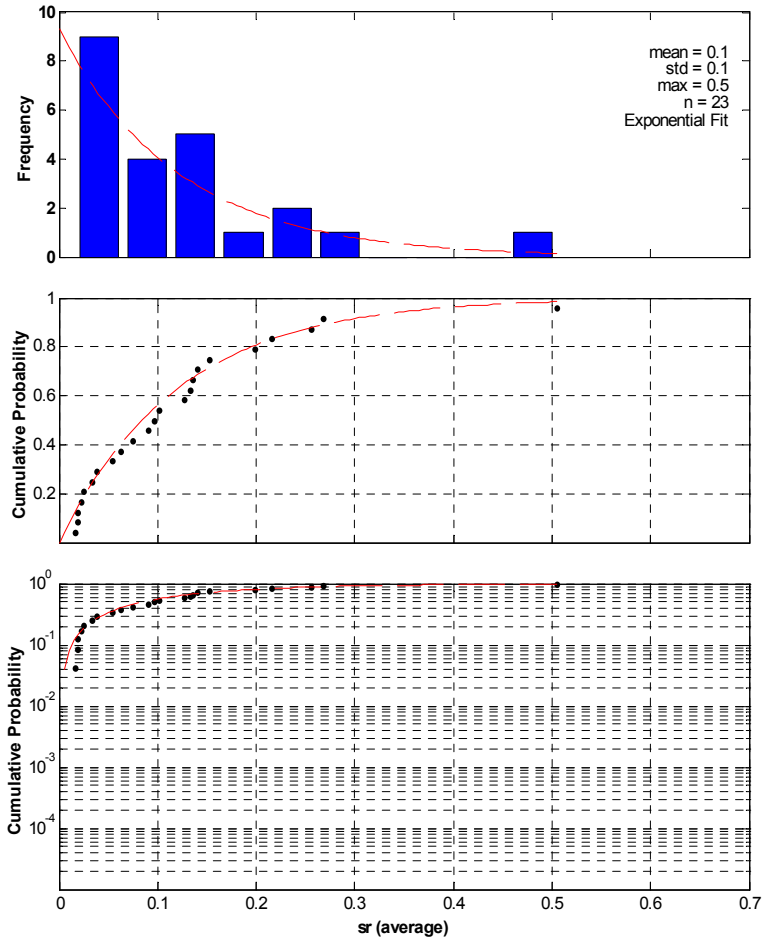

Figure 1: Probability distribution of sr_a and fitted Beta distribution

For this numerical exercise, the symmetric Beta probability distribution with parameters a = b = 1.5 were used for *sr*. "*sr*" should be correlated to slope angle; values in Table 2 show a positive correlation. Here, the lower bound value for the fitted probabilistic distribution of *sr* is taken as 0.1 or the *sr* corresponding to static *FS* = 1 if higher. The upper bound value of *sr* is taken equal to 0.35, as shown by the upperbound data set in Figure 50. This distribution is used for slope angles less than 16°, as there is a lack of data for areas of steeper slopes. It was considered that slope angles above 16°, that are stable under static conditions are likely to consist of stronger soil not representative of the conditions used. Slope angle, β and soil unit weight are assumed constant within any given deterministic exercise. The effects of natural soil variability are accounted for by using a characteristic strength value. Model uncertainty and bias are not included, for example correction of soil shear strength values obtained from laboratory vane shear tests.

With these assumptions annual probability of failure can be calculated:

$$p_f = \sum_L P[a > a_{crit}]P[a_{crit}]$$

where a is the earthquake horizontal acceleration; a_{crit} is the critical slope acceleration defined above; and L is the range of possible values of a_{crit}, which depends on the range of values of sr. To calculate p_f, range of values of sr are binned. For each value of binned sr, its binned probability and corresponding a_{crit} are calculated. From the hazard curve presented in Figure 49, the probability of an earthquake having an acceleration exceeding each a_{crit} is obtained. Probability of failure, then can be calculated using the above equation based on total probability theorem. Marcuson (1981) suggested that appropriate pseudostatic coefficients should correspond to one-third to one-half of the maximum acceleration for dams. Thus, the PGA values in Figure 49 are divided by a factor of 2.5 in this exercise. This approximately accounts for slope ductility after yield but would need to be verified for site specific conditions.

A probabilistic analysis was then performed for each grid point in the area being analysed. Rather than repeat the analysis for each grid point on the map, probability of failures were calculated for various slope angles from 0 to 16 degrees as shown in Figure 53. For each grid point, the probability of failure is interpolated based on its slope angle. Figures 54 and 55 show hazard maps for Scotian Shelf in terms of annual probability of failure using uncorrected and corrected slope angles respectively.

Similarly, analysis can be performed for a given earthquake design load (e.g. an earthquake with 10% probability in 50 years). For this, the above equation simplifies to:

$$p_f = \sum_{a_{crit} < a_{design}} P[a_{crit}]$$

where a_{design} is earthquake acceleration with the specified return period i.e. 10% probability in 50 years. Probability of failure, obtained here, shows values near to unity as shown in Figure 56. However, not all the slopes indicated would fail. For example, from comparison with field data, Jibson et al. (2000) found that only about one-third of slopes that are expected to fail, had really failed in 1994 Northridge earthquake. One of the main reasons for this may be a geometry that is incompatible with infinite slope analysis, eg. localized features.

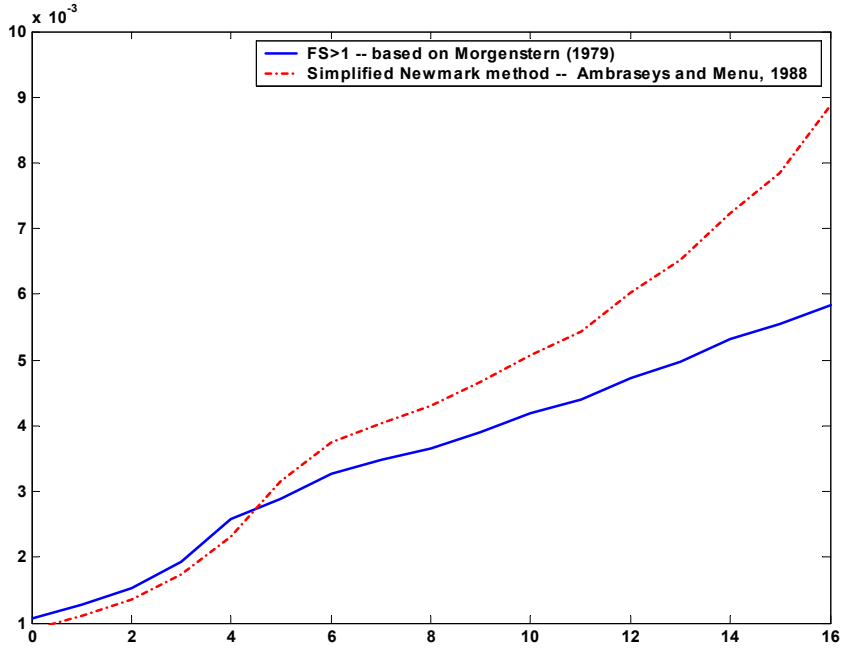

Figure 53: Probability of failure vs. slope angle

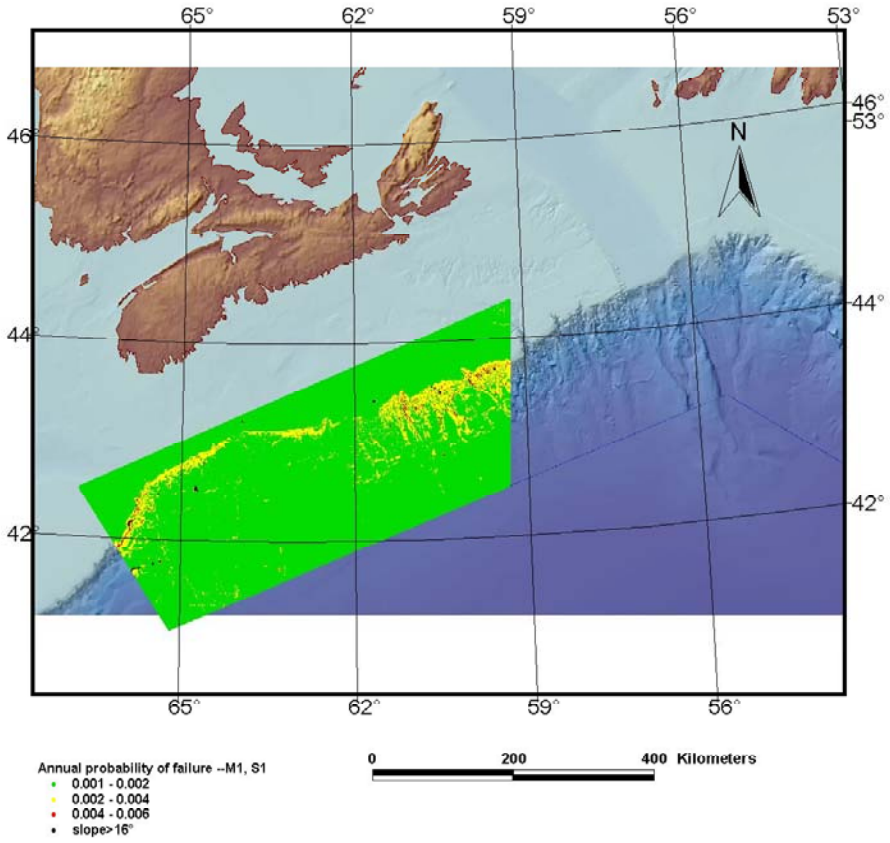

Figure 54: Hazard map showing annual probability of failure (uncorrected slope angles)

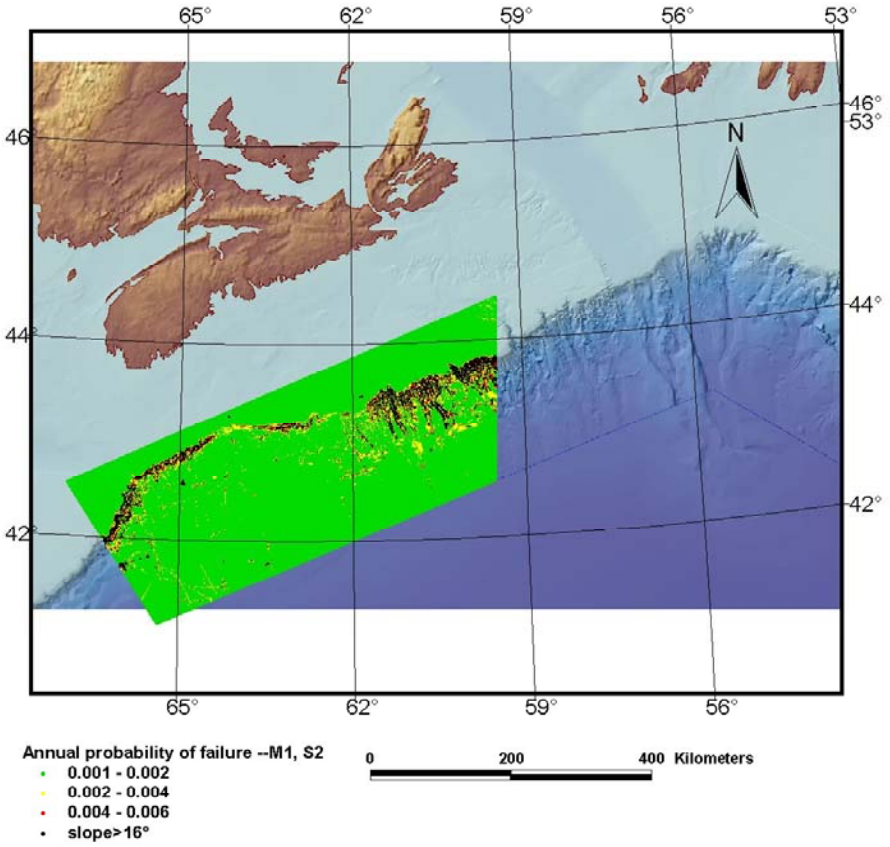

Figure 55: Hazard map showing annual probability of failure (corrected slope angles)

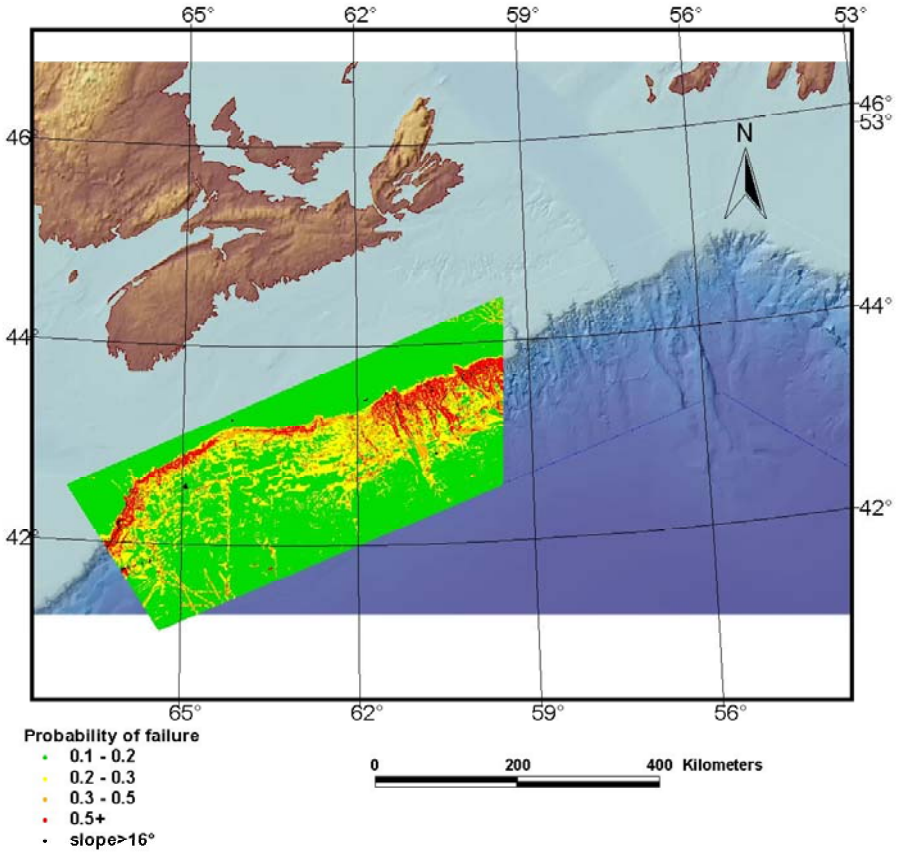

Figure 56: Hazard map showing probability of failure due to earthquake loading with 10% probability in 50 years

As an alternative approach, the Newmark method was also used to produce hazard maps, as described by Jibson et al. (1998 & 2000). They constructed an empirical slope fragility curve, which shows probability of slope failure (fragility) vs. Newmark displacement, by comparing calculated Newmark displacements with observed failure caused by the 1994 Northridge, California Earthquake. The relationship is:

$$p_f = 0.335[1 - e^{-0.048 D_n^{1.565}}]$$

where D_n is Newmark displacement. The factor "0.335", as accounts for the observation that not all the expected slopes failed due to factors which were not considered in the analysis (e.g. slope aspect and local geometry). Ambraseys and Menu (1988) calibrated the following equation for Newmark displacement:

$$\log D_n = 0.9 + \log\left[\left(1 - \frac{a_{crit}}{a_{\max}}\right)^{2.53}\left(\frac{a_{crit}}{a_{\max}}\right)^{-1.09}\right]$$

where a_{max} is peak horizontal acceleration. Based on total probability theorem. This can be rewritten as:

$$p_f = \sum_L \sum P\left[D > C \middle| D = D_n\right] P\left[D = D_n \middle| a = xa_{crit}\right] P\left[a_{crit}\right]$$

where $P\left[D > C \middle| D = D_n\right]$ is taken from P_f for a given value of D_n. In Figure 53, the dashed line shows annual probability of failure vs. slope angle using this method. Figure 57 shows the annual probability of failure obtained using this method over the analyzed domain. The factor "0.335" described above has not used in this exercise, as it was calibrated from specific onshore slopes with different soil properties and behavior.

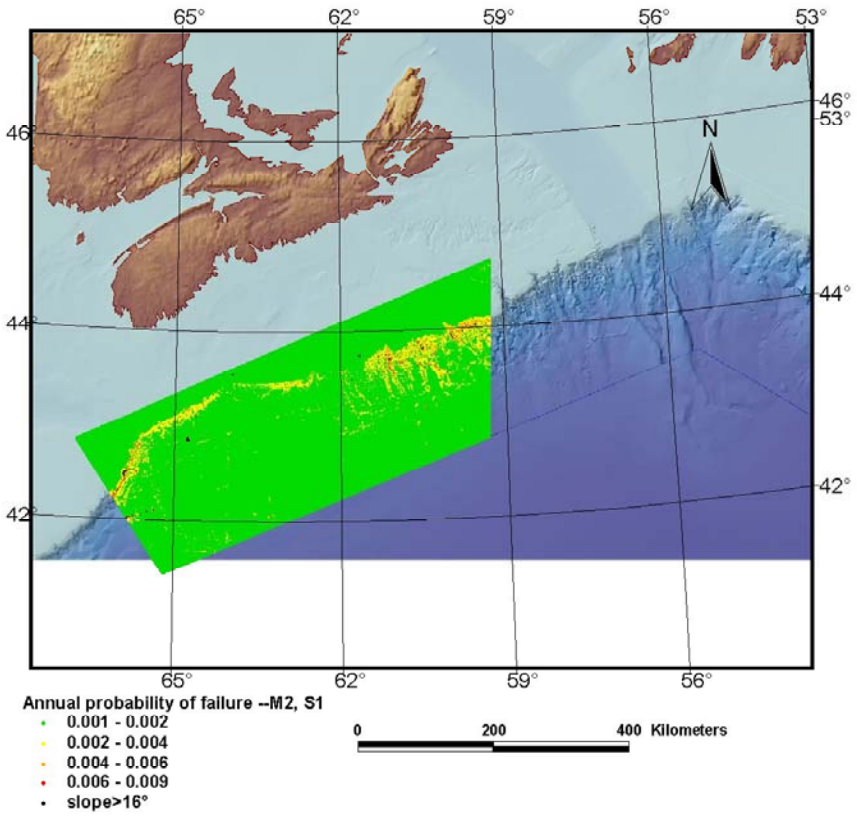

Figure57: Hazard map showing annual probability of failure using Newmark method (uncorrected slope angle)

4.6 Conclusions and Discussion

A methodology has been established to integrate topographic, geotechnical and environmental information and use them in probabilistic analysis to produce hazard maps. The methodology employs a probabilistic approach, which accounts for uncertainty in slope failure parameters as well as loading. The approach has been developed for earthquake loading, however it can be extended for use with other triggering mechanisms. The produced probabilistic hazard maps can be combined with associated hazard costs to perform risk analysis. The methodology has been demonstrated as an exercise to Scotian Shelf at this stage.

To produce realistic hazard maps, the following improvements can be sought:

- Significantly, more geotechnical data are required to establish reasonable soil zoning and layering in three dimensions. For example, the presence of loose sand layers depth may significantly affects failure mechanism and failure probability of a slope. Such a geotechnical investigation is probably only possible for much smaller areas of interest and for a specific construction development.

- An estimation of errors and bias in geotechnical parameters needs to be considered.

- The earthquake hazard curve and earthquake zoning could be improved and verified for specific locations. This would include a detailed zoning of areas of interest and construction of the corresponding hazard curves.

- Coarse slope angles, used in tbis exercise are not appropriate for a real engineering situation. A more accurate estimation of slope angles is recommended, although localized features analsyed using infinite slope analysis would produce conservative results.

- For earthquake loading, the peak ground acceleration may exceed critical acceleration of a slope by several times. However, this may not constitute a failure, but, depending on strain-softening properties, ductile yielding due to the short duration of loading events. To build reasonable failure criteria (limit state) or fragility curves, more detailed consideration should be given to the constitutive modeling of soil behavior.

Additional slope failure mechanisms which need to be addressed by this methodology include the analysis of erosion features and effects of pore pressure generation, from earthquake events and gas release. The effect of sedimentation rate could also be considered for areas where high rates are identified. The application of these mechanisms into the risk framework is ongoing.

5.0 REFERENCES

Adams. J., and Atkinson, G. (2003). Development of seismic hazard maps for the proposed 2005 edition of the National Building Code of Canada. Canadian Journal of Civil Engineering, 30, 255–271.

Adams, J., and Halchuk, S. (2003). Fourth generation seismic hazard maps of Canada: Values for over 650 Canadian localities intended for the 2005 National Building Code of Canada. Geological Survey of Canada, Open File 4459, 155 p.

Almeida, M.S.S. and Parry, R.H.G. (1985). Small Cone Penetrometer Tests and Piezocone Tests in Laboratory Consolidated Clays. Geotechnical Testing Journal. Vol. 8, No. 1. pp. 14-24.

Ambraseys, N.N., and Menu, J.M., 1988, Earthquake-induced ground displacements: Earthquake Engineering and Structural Dynamics, v. 16, p. 985-1006.

C-CORE (2002). Project Offshore Deep Slopes – Phase I. Final Report. Prepared for: Chevron Canada Resources, Pan Canadian, Murphy Oil, ExxonMobil, Minerals Management Services, Norsk Hydro and Statoil. Prepared by: C-CORE, OTRC, GSC and NGI. C-CORE Publication 01-C12.

Christian, John T.; Urzua, Alfredo (1998). Probabilistic evaluation of earthquake-induced slope failure. Journal of Geotechnical and Geoenvironmental Engineering, ASCE, Reston, VA, USA, 124(11), 1140-1143.

Davis, E. H. & Booker, J. R. (1973). The Effect of Increasing Strength with Depth on the Bearing Capacity of Clays. Geotechnique, 23, 4, pp. 551-265.

El-Ramly, H.; Morgenstern, N.R.; Cruden, D.M. (2002). Probabilistic slope stability analysis for practice. Canadian Geotechnical Journal, National Research Council of Canada, 39(3), 665-683.

Jibson, R.W., Harp, E.L., and Michael, J.A. (2000). A method for producing digital probabilistic seismic landslide hazard maps. Engineering Geology, 58, 271-289.

Kramer, S.L. (1996). Geotechnical Earthquake Engineering. Prentice Hall, 653 pages.

Marcuson, W.F., III (1981). Moderator's report for session on 'Earth dams and stability of slopes under dynamic loading'. Proceedings, International Conference on Recent Advances in Geotechnical Earthquake Engineeringand Soil Dynamics, St. Louis, Missouri, Vol. 3, p. 1175

Meyerhof, G. G. (1957). The Ultimate Bearing Capacity of Foundations on Slopes. Fourth International Conference on Soil Mechanics and Foundation engineering, London, Vol. 1, pp. 384-286.

Morgenstern, N.R. (1967). Submarine slumping and the initiation of turbidity currents. In Marine Geotechnique, Edited by Richards, A.F., page 189-220.

Nadim, F., Krunic, D., and Jeanjean, P. (2003). Probabilistic slope stability analyses of the sigsbee escarpment. Offshore Technology Conference, #15203.

Newmark, N.M. (1965). Effects of earthquake on dams and embarkments. Geotechnique, 15(2), 139-160.

Phoon, K.K., and Kulhawy, F.H. (1999a). Characterization of geotechnical variability. Canadian Geotechnical Journal, 36(5), 612-624.

Phoon, K.K., and Kulhawy, F.H. (1999b). "Evaluation of geotechnical property variability." Canadian Geotechnical Journal, 36(5), 625-639.

Tang, W. H. (1984). "Principles of probabilistic characterization of soil properties." Probabilistic Characterization of Soil Properties: Bridge Between Theory and Practice, ASCE, Atlanta, pp. 74-89.

Wu, T.H. and Abdel-Latif, M.A. (2000). Prediction and mapping of landslide hazard. Canadian Geotechnical Journal, 37, 781–795.

Zhou, G., Esaki, T., Mitani, Y., Xie, M., and Mori, J. (2003). Spatial probabilistic modeling of slope failure using integrated GIS Monte Carlo simulation approach. Engineering Geology, 68, 373-386.